Testing Mantle Convection Simulations with Paleobiology and Other Stratigraphic Observations: Examples from Western North America

Victoria M. Fernandes[1,2], Gareth G. Roberts[2], Fred Richards[2]

[1]GFZ Potsdam, Helmholtz Zentrum, Telegrafenberg, 14473 Potsdam, Germany
[2]Department of Earth Science and Engineering, Imperial College London, South Kensington Campus, SW7 2AZ, UK.

Key Points:

- Large-scale digital inventories of stratigraphic observations used to test predictions from mantle convection simulations.
- Useful diagnostics include net uplift and subsidence, absolute elevations, paleo-water depths.
- Upper mantle thermo-mechanical evolution—crucial for assessing sub-plate support—constrained using stratigraphy.

Corresponding author: V.M. Fernandes & G.G. Roberts, `milanez@gfz-potsdam.de`, `gareth.roberts@imperial.ac.uk`

Abstract

Mantle convection plays a fundamental role in driving evolution of oceanic and continental lithosphere. In turn it impacts a broad suite of processes operating at or close to Earth's surface including landscape evolution, glacio-eustasy, magmatism and climate. A variety of theoretical approaches now exist to simulate mantle convection. Outputs from such simulations are being used to parameterise models of landscape evolution and basin formation. However, the substantial body of existing simulations has generated a variety of conflicting views on the history of dynamic topography, its evolution and key parameters for modelling mantle flow. The focus of this study is on developing strategies to use large-scale quantitative stratigraphic observations to asses model predictions and identify simulation parameters that generate realistic predictions of Earth surface evolution. Spot measurements of uplift or subsidence provide useful target observations but are often controlled by tectonic processes, yet avoiding areas where tectonics have influenced vertical motions is challenging. To address this issue, we use large inventories of stratigraphic data from across North America with contextual geophysical and geodetic data to constrain the regional uplift and subsidence history. We demonstrate that a suite of fairly typical simulations struggle to match the amplitude, polarity and timing of observed vertical motions. Building on recent seismological advances, we then explore strategies for understanding patterns of continental uplift and subsidence that incorporate (and test) predicted evolution of the lithosphere, asthenosphere and deep mantle. Our results demonstrate the importance of contributions from the uppermost mantle in driving vertical motions of continental interiors.

1 Introduction

1.1 Overview

Mantle convection is generally accepted as an important driver of horizontal and vertical lithospheric motions (i.e., uplift and subsidence; *Pekeris*, 1935; *McKenzie & Jarvis*, 1980; *Parsons & Daly*, 1983; *Hager & Richards*, 1989; *Gurnis et al.*, 2000; *Hoggard et al.*, 2021). In turn, lithospheric motion in response to mantle convection appears to play a key role in driving diverse geological, geomorphological, glacio-eustatic and climatic processes (e.g., *Austernamm et al.*, 2015; *Salles et al.*, 2017; *Stephenson et al.*, 2019; *Richards et al.*, 2023). As such, there is considerable interest in developing reliable means to determine the history of mantle convection and its role in dictating the history of Earth's surface. An important challenge is to produce or identify data of sufficient quality and breadth such that histories of mantle convection can either be directly constrained, or used to test the fidelity of geodynamic simulations. In this contribution, we explore the use of substantial, digital, inventories of stratigraphic and paleobiological data to test vertical motion histories predicted by models of mantle convection. In our view, stratigraphic observations are the least equivocal constraints on histories of lithospheric vertical motion available and provide a crucial test of geodynamic simulations.

It is generally accepted that mantle convection is expressed in geological and geomorphological processes including the generation of topography (e.g., *Parsons & Daly*, 1983; *Richards & Hager*, 1984; *Hager & Richards*, 1985), creation of accommodation space in sedimentary basins (e.g., *Lodhia et al.*, 2018; *Morris et al.*, 2020), changes in sea-level (e.g., *Moucha et al.*, 2008), flooding of continental interiors and shoreline deformation (e.g., *Rowley et al.*, 2013; *Rovere et al.*, 2015). It also appears to determine the planform and relief of continental drainage patterns (e.g., *Cox*, 1989; *Roberts et al.*, 2012; *Czarnota et al.*, 2014; *Faccenna et al.*, 2019; *Lipp & Roberts*, 2021). In turn it likely impacts many related phenomena operating at, or close to, Earth's surface, including climate (*Conway-Jones & White*, 2022). Constraining amplitudes and histories of dynamic topography across scales of interest is clearly crucial for understanding Earth's surface evolution. For mantle convection, these scales include wavelengths, λ, set by the elastic strength of plates ($O(10{-}10^2)$ km), to global scales (spherical harmonic degree, $l = 2$, $\lambda = O(10^4)$ km; *Müller et al.*, 2018; *Ghelichkhan et al.*, 2021; *Holdt et al.*, 2022). Methodologies to constrain sub-plate support sit in two broad categories.

First, geological, geophysical and geomorphological observations have been used to constrain modern and historic dynamic topography at specific localities (e.g., *Fernandes et al.*, 2019; *Morris*

et al., 2020; *Ball et al.*, 2021; *Holdt et al.*, 2022). The clearest observational guide to amplitudes, wavelengths and spectral power of modern dynamic topography arise from fitting spherical harmonic functions to oceanic age-depth measurements (e.g., *Hoggard et al.*, 2020; *Valentine & Davies*, 2020; *Holdt et al.*, 2022, strictly, models are fit to residuals from calibrated oceanic plate cooling histories).

The second suite of methodologies use geodynamic simulators to predict dynamic topography across the scales of interest (e.g., *McKenzie et al.*, 1974; *Hager & Richards*, 1989; *Gurnis*, 1988; *Bunge & Baumgardner*, 1995; *Flament et al.*, 2013; *Colli et al.*, 2016; *Müller et al.*, 2018; *Ghelichkhan et al.*, 2021). This approach, which now often makes use of geological (e.g., plate motion histories) and geophysical (e.g., seismic tomography) observations and theory to prescribe model properties (e.g., conversion of acoustic velocities into density), provides means to explore theoretical expressions and sensitivities of dynamic topography to calculated mantle evolution (e.g., *Flament et al.*, 2013; *Müller et al.*, 2018). There now exists a considerable body of mantle convection simulations, a few of which have been compared to independent geological observations at specific localities (e.g., New Jersey Margin, North America; *Flament et al.*, 2013) and to global power spectra of ocean age-depth residuals (*Hoggard et al.*, 2016). Model predictions, such as uplift and subsidence, have recently been coupled with models of lithospheric and landscape evolution to predict development of drainage networks and sedimentary basins (e.g., *Salles et al.*, 2017; *Faccenna et al.*, 2019; *Wang et al.*, 2020; *Ding et al.*, 2023).

Assessing sub-plate support of continents is generally more challenging than for oceans. The variability and complexity of continental lithosphere rheology, structure, and density tend to make extricating patterns of dynamic topography fraught (see, e.g., *Hoggard et al.*, 2021; *Stephenson et al.*, 2021). Nonetheless, assessing predictions, and changes, of continental sub-plate support has recently become considerably more tractable due to the improved availability of stratigraphic data (e.g., Macrostrat, Paleobiology Database). These data can be combined with geophysical observations (e.g., seismology; gravity anomalies) as well as other geological (e.g., magmatic) and geomorphological observations to constrain geometries and histories of sub-plate support (e.g., *Fernandes & Roberts*, 2021). As an example, in this paper we focus on Western North America, where stratigraphic data is dense and well documented. Additionally, a large body of magmatic and geophysical data is available to test predictions of mantle convection simulations. A considerable body of information regarding contextual tectonic histories (e.g., crustal shortening, extension and plate flexure) also exists, which is crucial for extricating signals of sub-plate support from geological observations (e.g., *DeCelles*, 1994).

Available stratigraphic observations include paleo-water depth information recorded in the Paleobiology Database (PBDB), developed by the paleobiological community, and stratigraphic data that record transitions from marine to terrestrial deposition (e.g., *Hintze and Kowallis*, 2009). These data have the important benefit of requiring few corrections, bar minor, relatively well constrained adjustments for compaction and denudation (see, e.g., *Fernandes & Roberts*, 2021). There are of course many other indirect constraints on lithospheric vertical motions including thermochronometry, palynology, isotopes, histories of sedimentary flux, and landform geometries, which can be used to fill in spatio-temporal stratigraphic gaps (e.g., *Flowers et al.*, 2008; *Huntington et al.*, 2010; *Galloway et al.*, 2011; *Flowers et al.*, 2012; *Flowers and Farley*, 2012; *Roberts et al.*, 2012; *Chamberlain et al.*, 2012; *Blum and Pecha*, 2014; *Fernandes et al.*, 2019). However, we think it is important to make a distinction between information provided from such approaches and the more direct constraints on elevation, uplift and subsidence that arise from interrogating the stratigraphic archive.

In the following sections, first, existing geological constraints on the history of vertical motions of the North American Western Interior are summarised. Secondly, predictions of dynamic topography from mantle circulation models are compared to geological observations. We identify model parameterizations that best match geological observations. Thirdly, geophysical observations of the upper mantle are combined with isostatic models to explore asthenospheric and lithospheric contributions to uplift in the region. We note that evolution of the uppermost convecting mantle and lithosphere are sometimes not included in global geodynamic simulations, including those assessed in this paper. The isostatic models we develop make use of seismological and stratigraphic observations to explore contributions to North American topography from asthenospheric thermal anomalies and modification of lithospheric depletion and structure. Finally, we quantify uncertainties and

sensitivities via Monte Carlo error propagation, and discuss the implications of findings for assessing predictions of dynamic topography from geodynamic models.

1.2 Global observations of sub-plate support

Potential field and seismological observations combined with magmatism, geomorphology and stratigraphy have been used to quantify modern sub-plate support and histories of dynamic topography (e.g., *Gurnis*, 1990; *Gurnis et al.*, 2000; *Roberts et al.*, 2012; *Klöcking et al.*, 2018; *Stephenson et al.*, 2019; *Ball et al.*, 2021). The relative simplicity and consistency of oceanic lithospheric structure and rheologies, combined with increasingly tightly constrained thermal histories, make it well suited for identifying signals of sub-plate support. For example, the age and isostatically corrected basement depths of oceanic basins have been used to measure residuals from ocean plate cooling models with amplitudes up to O(1) km (e.g., *Menard*, 1969; *Crough*, 1983; *Panasyuk & Hager*, 2000; *Hoggard et al.*, 2016; *Richards et al.*, 2020; *Valentine & Davies*, 2020). A recent, extensive, compilation of measurements across all oceanic basins indicates that residual surface deflections are measurable to wavelengths at least as low as $\sim$ 900 km (spherical harmonic degree 40; *Holdt et al.*, 2022). These near global-scale compilations of residual topography paint a detailed picture of the present-day state of dynamic topography along continental margins and within oceanic basins. The power spectra of oceanic residual depths indicate that both deep mantle flow and shallower processes, likely involving interaction between the asthenosphere and lithosphere, are fundamental for generating Earth's dynamic surface response. Deep mantle flow primarily contributes to dynamic topography at long wavelengths ($\sim 10^4$ km), and shallower processes control shorter wavelength contributions (10^2–10^3km; *Parsons & Daly*, 1983; *Colli et al.*, 2016; *Richards et al.*, 2020). As an example, consider Atlantic oceanic lithosphere abutting eastern North America, which has residuals of up to $\pm$1 km (*Holdt et al.*, 2022). Backstripping of stratigraphy preserved along this passive margin indicates that sub-plate drawdown generated 500–900 m of water-loaded subsidence during the last $\sim$ 20 Ma (*Morris et al.*, 2020).

Global compilations of melt fractions of young (Neogene-Quaternary) mafic rocks and upper mantle shear wave velocity anomalies have recently been shown to be broadly negatively correlated (*Ball et al.*, 2021). For example, mafic samples in western North America are concentrated atop slow upper mantle shear-wave velocity anomalies. Many continental regions underlain by relatively slow upper mantle shear wave velocity anomalies, including Western North America, are also associated with uplifted marine rock (*Fernandes et al.*, 2019). Such stratigraphy, preserved atop continental interiors and on fringing sedimentary basins, provides opportunities to constrain histories of sub-plate support (*Fernandes & Roberts*, 2021). Elevated Quaternary marine terraces and warped shorelines provide the least equivocal constraints on vertical lithospheric motions, but are limited to the more recent geological past (e.g., *Austermann et al.*, 2017). Older paleo-water depth indicators preserved in the marine rock record can be used to extend these constraints further into the geological past (e.g., *Dickinson et al.*, 1988; *Bessin et al.*, 2017). A general challenge is generating observations at sufficient scale and density to directly constrain histories of sub-plate support at O(10^2–10^3) km wavelengths. Building on the methodologies developed by *Ziegler et al.* (1985), *Sahagian* (1988) and *Rowley et al.* (2013), *Fernandes & Roberts* (2021) generated an inventory of 24,372 measurements of Late Cretaceous to Recent net uplift. These measurements were generated by combining records of Cretaceous to Recent marine rock documented in the Paleobiology Database (PBDB) with estimates of elevation, paleobathymetry, compaction, and global sea-level change. The distribution of recorded marine rock is of course not uniform across all continents. Nonetheless, most continents have stratigraphic observations preserved in sedimentary basins and atop uplifted topography that are suited to testing predictions of geodynamic models.

1.3 Geodynamic modelling

A variety of methodologies exist to retrodict mantle convection. A widely used approach inverts mantle structure derived from seismological (tomographic) models of Earth's interior, and can incorporate supplementary information (e.g., plate motion histories). Methods for prescribing temperature, density and viscosity fields, and also surface velocities, that drive mantle convection simulations vary (see e.g., *Hager & Richards*, 1985; *Gurnis*, 1990; *Forte*, 2000; Forte et al., 2007; *Forte*

et al., 2009; Forte et al., 2010; *Spasojević & Gurnis*, 2012; *Flament et al.*, 2013; *Müller et al.*, 2018; *Ghelichkhan et al.*, 2021). As such, associated models have differing predictive capabilities. Some constrain the present-day state of the mantle and its rate of change, whilst those generated using adjoint or data assimilation methods make predictions of how dynamic topography has changed in the geological past (see, e.g., *Ghelichkhan et al.*, 2021). We note that a significant number of mantle convection simulations do not include the shallowest 200–350 km of the mantle in part because of the computational challenges associated with accurately modelling large changes in viscosity between the lithosphere and asthenosphere, uncertain lithospheric structure and rheologies, and difficulty of accurately incorporating boundary conditions on numerical simulations. This approach makes it challenging to ascertain the role the dynamic shallow mantle plays in generating topography. Given that simulations of mantle convection are often extremely computationally expensive, we think it is prudent to develop strategies to identify existing simulations that are consistent with available observations.

Here, we focus on testing predictions generated by *Müller et al.* (2018) because they examined a diverse range of parameterisations, and made their predictions available for testing. We use their outputs in a plate reference frame. A focus of this study is on examining whether contributions from the uppermost convecting mantle and lithosphere, which might include isostatic effects associated with heating asthenosphere and changes in lithospheric mantle thickness or density, are crucial for generating observed vertical lithospheric motions (e.g., *Colli et al.*, 2016). First, we explain why Western North America was chosen to test model predictions.

2 North American dynamic topography: Observations and theory

2.1 Geophysical and stratigraphic framework

A considerable body of geophysical and geological data across North America constrains the present-day state of its crust, lithospheric and sub-lithospheric mantle, and therefore isostatic contributions to topography, with higher fidelity than most places on Earth. These include, but are not limited to USArray-derived seismic velocities of the crust and mantle, active source seismology, gravity anomalies and associated estimates of elastic thickness and dynamic support, and stratigraphic observations (see, e.g., *Crough*, 1983; *Laske et al.*, 2013; *Buehler & Shearer*, 2016; *Fernandes & Roberts*, 2021; *Hoggard et al.*, 2021). Additionally, isotopic paleoaltimetry, thermochronometry, sedimentary flux histories, mafic melting histories, and geomorphic observations and theory provide contextual information about the evolution of North American topography and sub-plate support (see, e.g., *Fernandes et al.*, 2019, for summary). Inverse modelling of longitudinal river profiles provides one way to fill spatio-temporal gaps between spot measurements (e.g., *Roberts et al.*, 2012; *Fernandes et al.*, 2019). Nonetheless, disentangling tectonic (e.g., shortening, extension) and sub-lithospheric contributions to elevations is especially fraught along the western continental margin where tectonic processes and terrane accretion have dominated its recent geological history. Instead, we focus on Cretaceous to Recent stratigraphy in the North American Western Interior (Figure 1).

In our view, the least equivocal, most direct, constraints on histories of North American vertical lithospheric motion arise from the distribution of ancient marine rock (e.g., *Ziegler et al.*, 1985). Biostratigraphic information contained within these rocks (e.g., age, paleo-water depth) provide crucial clues about the elevation of Earth's surface at specific times, typically when it is at, or close to, sea-level. By combining these data with their compaction and denudation histories, spot measurements of post-deposition uplift can be generated for substantial tracts of North American topography (*Fernandes & Roberts*, 2021). The present-day elevation of marine fossil assemblages recorded in the PBDB, for example, provide constraints on post-Cretaceous net uplift in the Great Plains, Rocky-Mountains-Colorado-plateaux, Basin and Range, and Interior Lowlands (Figure 1). In addition, stratigraphic sections throughout North America record facies transitions from marine to non-marine depositional environments, which can be used to calculate precise rates of net uplift (e.g., *Hintze and Kowallis*, 2009; *Hampson*, 2010). Building on the body of stratigraphic observations generated by *Crough* (1983), *Ziegler et al.* (1985) and others, *Fernandes et al.* (2019) compiled 339 locations where such stratigraphic transitions are observed in outcropping stratigraphy of the North American Western Interior. Stratigraphy from these locations typically feature as part of well-established chronos-

tratigraphic frameworks that include radiometric dating (*Obradovich & Cobban*, 1975; *Cobban et al.*, 2006; *Merewether et al.*, 2011; *Merewether & McKinney*, 2015; *Lynds & Slattery*, 2017). Thicknesses and distributions of Cretaceous rocks from outcrop and well data (e.g., Mancos Shale) are of special importance because of their role in defining when marine conditions likely last prevailed across large tracts of the continental interior (*Bond*, 1976; *Cross and Piliger*, 1978; *Roberts & Kirschbaum*, 1995; *Li & Aschoff*, 2022).

The subsidence history of the region is also well documented from well and outcrop data. Tectonic processes (lithospheric shortening, extension, plate flexure) evidently generated Cretaceous to Recent accommodation space and uplifted sedimentary rock (e.g., in the Basin and Range province, Rio Grange Rift, Sevier-Laramide piggy-back basins and forelands; *Cross and Piliger*, 1978; *Cross*, 1986; *Dickinson et al.*, 1988; *Dickinson*, 2004). For example, during Cretaceous flooding > 12 km of sediment was deposited in small, isolated, probably flexural basins (e.g., *Roberts & Kirschbaum*, 1995). Nonetheless, the distribution of uplifted marine rock and subsidence patterns indicate that such tectonic processes cannot explain $O(1)$ km subsidence at horizontal scales > 1000 km. Instead, mantle convective drawdown likely played an important role in generating accommodation space at these scales (e.g., *Mitrovica et al.*, 1989; *Pang & Nummedal*, 1995). In this paper we explore how such observations of net vertical lithospheric motion can be used to assess predictions from geodynamic models.

2.2 Quantifying net vertical motions from stratigraphy

2.2.1 Uplift

We quantify uplift using the data compilations of marine fossil assemblages with a known paleo-water depth, and stratigraphic markers of the youngest outcropping transition between marine and non-marine depositional environments presented in *Fernandes et al.* (2019) and *Fernandes & Roberts* (2021). Together, these constraints comprise > 2000 spot measurements of net uplift. Regressive stratigraphic sequences were identified from published facies interpretations (e.g., *Roberts & Kirschbaum*, 1995; *Johnson et al.*, 2002; *Gani et al.*, 2015), and ages were tied using published regional chronostratigraphy (Figure 1D; *Obradovich & Cobban*, 1975; *Cobban et al.*, 2006; *Merewether et al.*, 2011; *Merewether & McKinney*, 2015; *Lynds & Slattery*, 2017). Particular care was taken to identify lateral and temporal variability in the depositional facies sequences. Depositional environments, interpreted using fossil assemblages, were converted to paleo-water depth using the paleo-bathymetric model described by *Fernandes & Roberts* (2021, Figure 1E). Elevations and paleo-sea level ranges were extracted from ETOPO1 and the compilation of *Bessin et al.* (2017), respectively.

A demonstration of the methodology for estimating net uplift from fossil assemblages is shown in Figure 2. This figure shows net uplift of a fossil assemblage from the Book Cliffs Utah corrected for paleo-water depth, sea-level and compaction. Net dynamic topography extracted from Model M2 of *Müller et al.* (2018) is also included to illustrate our approach to extracting commensurate (in time) predictions.

The spatial and temporal distribution of paleo-biological data provide constraints on the magnitude of net uplift experienced at each location, and paleo-elevation of the surface at the time of deposition. This information constrains both the absolute paleo-elevation of the region, as well as the magnitude and polarity of net post-deposition vertical motion. Using such inventories of geological observations means that suites of spot measurements can be used to identify vertical motions associated with changes in elevation at the scales predicted by mantle convection models (e.g., $>$ 1000 km; i.e., larger than deflections determined by flexural rigidity of the lithosphere). The fossil and stratigraphic dataset we make use of covers 3500×2350 km, with a sample density of ~ 1 sample per km in the densest regions (Figure 1D).

There are a variety of means to assess long wavelength contributions to measured uplift (e.g., fitting spherical harmonic functions to spot measurements; *Hoggard et al.*, 2016). Given that we focus on a single continental region, a simple way to do so is to fit splines to spot measurements. We seek gridded surfaces that require the least smoothing of data and allow the amplitude of measurements to be preserved (Figure 1). The resultant grid was filtered using a 1000-km low-pass Gaus-

sian filter and is shown in Figure 3A. A histogram showing the difference between the grid and spot measurements of uplift is shown in Figure 3B. The difference between the smooth surface and spot measurements is less than ±200 m for > 65% of the spot measurements, which we attribute to large-scale, > 1000 km, post-deposition uplift. Small-scale deviations from the large-scale pattern of uplift are generally associated with small-scale faulting generated principally during Laramide deformation and basin-forming tectonic events (see, e.g., *Dickinson et al.*, 1988; *DeCelles*, 2004). Grids generated using alternative low-pass cut-offs are shown in Supplementary Figure S1.

2.2.2 Subsidence

Additional constraints on the vertical motions of Western North America were provided by the subsidence history of the Western Interior Basin. Basin stratigraphy recorded in individual wells has been flexurally backstripped to reveal a spatially and temporally variable subsidence pattern (see Supplementary Figures S3-5; *Liu et al.*, 2014). However, individual wells do not constrain the history of subsidence on a sufficiently large scale to accurately reflect the broader geodynamic history of the basin. In order to expand this dataset to larger spatial scales, following *Mitrovica et al.* (1989), we calculate subsidence by backstripping existing regional isopach maps. First, isopach maps from *Roberts & Kirschbaum* (1995) were digitised using QGIS software. The published isopach figures for each time slice were geo-referenced, and contour lines were individually traced to create a vector map of the contour lines where the thickness value of each line is an attribute. Next, using GRASS functionalities, the vector map was rasterized by creating a 10 × 10 minute grid, where each grid cell is either a contour line cell (containing the sediment thickness value), or a fill cell. Using the r.surf.cont functionality, a linear interpolation between contour intervals was performed using a flood fill algorithm. Gridding by fitting a regularised spline with tension was also tested, however this methodology produced unwanted data artefacts in regions where the contour lines were too closely spaced. The best-fit isopach maps are shown in Supplementary Figure S3.

Air-loaded subsidence histories were calculated by backstripping the isopach maps. Admittance between gravity and topography, and their associated coherence, indicates that the elastic thickness of the lithosphere, T_e, beneath the North American Western Interior is < 40 km and as low as ∼ 10 km atop the Colorado Plateau (*Stephenson et al.*, 2014; *Audet*, 2014). These results suggest that it is reasonable to assume isostasy prevails when backstripping. The isopach maps were decompacted using the compaction parameterisation of *Athy* (1930). We assumed a compaction wavelength $\lambda =$ 2 km and initial porosity $\phi_\circ = 0.6$, typical for sandstones (*Sclater & Christie*, 1980). Minimum and maximum subsidence was calculated by assuming 0 and 3 km thickness of post-Cretaceous sediment was preserved atop Cretaceous rock, respectively. Maximum thickness of post-Cretaceous rocks were estimated from an average thicknesses preserved in boreholes and outcrops in the area (e.g., *Hintze and Kowallis*, 2009). In order to compare the subsidence histories with dynamic topography predictions, decompacted subsidence was isostatically air-loaded assuming a density of sedimentary rock, $\rho_s = 2400$ kg m^{-3}. The resultant grids of calculated subsidence are shown in Supplementary Figure S4 and are summarised for specific localities of interest in Figure 6. These maps are in broad agreement with previous studies, providing a large-scale spatio-temporal history of subsidence (see *Cross and Piliger*, 1978; *Mitrovica et al.*, 1989). The pattern and magnitude of subsidence predicted from this simple method was compared to subsidence estimates for the same time intervals generated from backstripping of data from individual wells (colored circles in Figure 6; *Liu et al.*, 2014). There is generally a good agreement between the well data and the subsidence grids, both in the spatial distribution and the magnitude of subsidence.

The results suggest that parts of the westernmost portion of the study region, i.e., the Basin and Range and Colorado Plateau, experienced subsidence due to lithospheric thinning and loading. Backstripping of well data predict a higher magnitude of subsidence in the Late Campanian, which is likely due to a combination of grid smoothing and choice of compaction parameterisation. We now have a body of uplift and subsidence data from across Western North America with which we can test predictions from geodynamic simulations of mantle convection.

3 Testing histories of dynamic topography from mantle convection simulations

3.1 Introduction

A substantial body of published mantle convection simulations predict dynamic topography of Western North America (see, e.g., Forte et al., 2007; *Liu et al.*, 2008; *Moucha et al.*, 2008; *Forte et al.*, 2009; *Flament et al.*, 2013; *Liu et al.*, 2014; *Rovere et al.*, 2015; *Müller et al.*, 2018; *Davies et al.*, 2023). We focus on testing predictions of dynamic topography from the eight models presented by *Müller et al.* (2018). Their paper describes their methodologies in depth and clearly explains challenges and potential pitfalls in comparing models predictions to independent geologic observations. An important issue they discuss, which we address below, is exclusion of the upper few hundred kilometres of the Earth from calculations of dynamic topography. In short, they test different parameterisations including variations in viscosity, thermal expansivity, density, activation energies and initial conditions. They also test models that contain plumes and models in which plume formation is suppressed. The models can be placed into three categories based on their parameterisations, each of which make broadly similar predictions: M1, M2–M4 and M5–M7. In model M1 mantle flow is computed by a backwards integration of the temperature field wherein the direction of gravity and plate motions are reversed (*Liu et al.*, 2008; *Spasojević & Gurnis*, 2012). The other models are driven by forward thermal convection with plate velocities applied as surface boundary conditions using a modified version of CitcomS (*Müller et al.*, 2018). The main difference between the M2–M4 and M5–M7 families of models lies within their viscosity structures; M5–M7 models have mantle viscosities that are lower by $O(10{-}10^2)$, and a much larger viscosity contrast between the lithosphere and asthenosphere (asthenosphere viscosity being 500× lower, when compared to 10× lower in models M2–M4). For all models, average model resolution is 50×50×15 km at Earth's surface. Predicted dynamic topography and its incremental change for each model is shown in the Supplementary Information.

Examples of predicted net change in dynamic topography from each category are shown in Figure 4A–C. Grids of calculated net dynamic topography were generated by subtracting values from a specific time in the past (e.g., 90, 80, 70 or 60 Ma) from present-day values (see, e.g., Figure 4A). By doing so we can compare changes in predicted dynamic topography to net uplift or subsidence recorded by stratigraphy. Each group of models generated significantly different predictions of the history, spatial distribution and amplitude of dynamic topography. We compare absolute elevations and net vertical motions recorded by stratigraphy to predictions of net dynamic topography.

3.2 General insights from testing geodynamic predictions using geologic observations

Müller et al. (2018) compared their dynamic topographic predictions to power spectra of ocean-age depth residuals and to paleo-geographic maps generated by, e.g., *Smith et al.* (1994) and *Heine et al.* (2015). Most of the models over-predict power calculated from ocean-age depth residuals at spherical harmonic degrees 1–2 (wavelengths $\sim 2.2{\pm}0.6{\times}10^4$ km; see their Figure 5), despite having excised the top 300 km of the upper mantle containing strong long-wavelength anomalies. Models M5–7 most closely match spectra of residual depth anomalies at degrees 2–3 ($\lambda = 1.4 \pm 0.3 \times 10^4$ km), but under-predict power at higher degrees. Models M1–4 more closely match at degrees 3–5 ($\lambda = 0.9 \pm 0.2 \times 10^4$ km). In other words, none of the models match the entire power spectrum of ocean age-depth residual at degrees 1–5, but some do a reasonable job at specific scales. Paleogeographic maps were also used to identify regions submerging or emerging from beneath sea-level at given time periods. These data were used to constrain the polarity of vertical lithospheric motions (i.e., uplift or subsidence). Their preferred model, which most closely matches continental inundation by seaways, is the forward geodynamic simulation M7, which suppresses plumes. We explore whether amplitudes and net change in vertical lithospheric motion provide additional useful information to discriminate between models. In this study, we test the model predictions using geological observations in three ways.

First, amplitude and polarity of net dynamic topographic change since the Late Cretaceous are compared to spot measurements from the PBDB augmented by 339 spot measurements that tightly constrain the timing of transition from marine to terrestrial conditions. We select eight specific lo-

374 calities with different tectonic and lithospheric settings across the continent to demonstrate our ap-
375 proach (Figure 1). The seven geodynamic models predict net uplift for most of the North Ameri-
376 can Western Interior since the late Cretaceous, however the pattern and amplitude of uplift signif-
377 icantly vary between models. As an example of the diversity of model predictions, consider Figure
378 4D–G, which shows calculated dynamic topography in Alberta, Manitoba, Utah and New Mexico
379 (see Figure 4A). Predicted net dynamic topography was extracted at the same location and for the
380 same duration as each PBDB and stratigraphic constraint (see, e.g., Figure 2).

381 Second, predictions of the absolute amplitude of dynamic topography in the Late Cretaceous
382 are compared to paleo-water depth estimates from the PBDB and additional stratigraphic constraints.
383 Air-loaded predictions of dynamic topography from the geodynamic models (D_{air}) were isostatically
384 corrected to a water-load (D_w),

$$D_{air} = D_w \frac{\rho_a}{\rho_a - \rho_w} \approx 1.43 D_w \tag{1}$$

385 where ρ_a and ρ_w is the density of asthenospheric mantle and water, respectively. To extract predicted
386 water-loaded dynamic topography at a specific time (e.g., the time of deposition of the fossil assem-
387 blage in Figure 2, 81.22 Ma) the discrete time steps (e.g., 80, 90 Ma) of *Müller et al.* (2018) were
388 linearly interpolated (see blue line in Figure 2D). Thus, predicted dynamic topography at the lo-
389 cation and time of deposition of each fossil assemblage was extracted and compared to the observed
390 paleo-bathymetry (interpreted from the fossil record).

391 Finally, the history of Late Cretaceous dynamic topographic vertical motions are compared
392 to the subsidence history of the Western Interior Basin. Figure 6 shows the Late Cretaceous ver-
393 tical motions at four key locations (shown in Figure 4A). For each location, the first panel shows
394 paleo-water depth of fossil assemblages located within a 50 km radius of dynamic topography pre-
395 dicted by the geodynamic models. The second panel shows the predicted net change in dynamic to-
396 pography for each Late Cretaceous stage: Cenomanian, Turonian, Santonian–Coniacian, lower Cam-
397 panian, upper Campanian and Maastrichtian. The final panel shows the range of isopach thicknesses
398 within a 50 km radius of the point, isostatic subsidence from backstripping the isopach maps of *Roberts*
399 *& Kirschbaum* (1995), and a subsidence curve from *Liu et al.* (2014). In all cases, the continuous
400 subsidence of the Western Interior Basin in the Late Cretaceous requires that the net vertical mo-
401 tion of the surface is negative. However, with the exception of point 8, located in the eastern-most
402 edge of the Western Interior Basin, all models predict dynamic uplift of the North American West-
403 ern Interior in the Late Cretaceous.

404 In the following subsections we summarise the specific parameterisations, described in detail
405 by *Müller et al.* (2018), and predictions from each group of models. The fidelity of predicted dynamic
406 topography is then assessed by comparison to the inventory of stratigraphic data.

407 3.3 Geodynamic Model M1

408 Model M1 uses the plate reconstruction of *Gurnis et al.* (2012), and is equivalent to the hy-
409 brid model of *Spasojević & Gurnis* (2012, their model *M2*). The global mantle temperature field at
410 present-day is estimated using tomographic inversions of different seismic phases (surface and body
411 waves using the S20RTS model in the lower mantle, and Benioff zone seismicity for the upper man-
412 tle). The temperature field is back-integrated using the backward integration method of *Liu & Gur-*
413 *nis* (2008). A hybrid paleo-buoyancy field is generated by merging the calculated backward-advected
414 mantle temperature field with synthetic subducted slabs assimilated into the model based on loca-
415 tion of subduction zones (*Spasojević & Gurnis*, 2012). The model has a Rayleigh number, $Ra = 7.5\times10^7$. Air-loaded dynamic topography is calculated with a no-slip surface boundary condition,
416
417 with the top 250 km of mantle removed from the calculation. The power spectra of dynamic topog-
418 raphy predictions show that model M1 has the highest power at spherical harmonic degree $l = 1-3$
419 for all examples considered by *Müller et al.* (2018). It predicts highest amplitudes of dynamic to-
420 pography at wavelengths $> 10,000$ km. Comparisons between observed and predicted net vertical
421 motions since 85 ± 5, 75 ± 5, 65 ± 5 and < 60 Ma are shown in Figure 5A. For each scatter plot, a

linear regression was fit using a least-squares residual misfit calculation and 99% confidence interval. Model M1 tends to under-predict net uplift of Cretaceous to earliest Cenozoic marine rocks. Observed and predicted paleo-water depths for model M1 are shown in Figure 5E–H, along with a least-squares regression fit through the data. The range of predicted Cretaceous to Cenozoic water-loaded elevations is somewhat larger than those constrained by biostratigraphic data. However, we note that many of the points coincide with the 1:1 line within error.

3.4 Models M2-M4

Models M2–M4 are characterised by initial conditions that include a 113 km thick basal thermochemical layer above the core-mantle boundary (CMB) that is 4.2% denser than ambient mantle, which acts to suppresses plume formation. This dense basal layer has the same thickness as the lower thermal boundary layer. They explore the consequences of assuming constant thermal expansion and temperature-dependent viscosity. The models have a $Ra = 7.8{\times}10^7$. Model M2 uses the plate reconstruction of *Seton et al.* (2012), and is equivalent to Model 3 from *Müller et al.* (2016a). Model M3 uses the plate reconstruction of *Müller et al.* (2016a) and is equivalent to Model 2 described in *Müller et al.* (2016a). Model M4 uses the relative plate motions of *Müller et al.* (2016a), absolute plate velocities of *Van der Meer et al.* (2010), and is equivalent to model (case) 24 from *Flament et al.* (2017).

For models M2–4 (and M5–7), dynamic topography is calculated from surface vertical stress resulting from mantle flow in restarts of the model in which the surface boundary condition is free-slip and top 350 km is removed from the calculations. Lateral viscosity variations are preserved in the rest of the mantle. The power spectra of predicted dynamic topography from all models show that for models M1–M4 the highest power resides at spherical harmonic degree $l = 2$.

The amplitude of observed net uplift is best matched by models M2, M3 and M4 (see Figure 10C). These models predict a large amplitude drawdown at ~ 90 Ma, ranging from -1.5 km to -4 km, and subsequent net uplift to ~ 0 km at present day. Uplift is highest in the West (Arizona, Colorado, Wyoming) with a smooth decrease to the East (Illinois, Wisconsin). If all of the uplift was dynamic in origin, these results would suggest that the present-day topography of the North American Western Interior may not be dynamically supported, but instead owes its history of vertical motions to recovery from Cretaceous drawdown caused by subduction of the Farallon slab (*Spasojević & Gurnis*, 2012). As such, any additional sources of vertical motions would be negligible. Models M2–M4 predict as much as 1.5 km of uplift near the Colorado Plateau (near the Utah-Colorado border) during Santonian-Coniacian times (83.6–89.8 Ma). Conversely, the stratigraphic record indicates water-loaded subsidence of $\sim 100 - 500$ m and up to 1.5 km of sediment accumulation during this time. As far as we are aware, there is no evidence for a widespread stratigraphic unconformity that might be expected to have been generated as a consequence of 1.5 km of regional uplift during this time.

M2–M4 predict up to ~ 1 km of water-loaded Cretaceous subsidence, with a sharp uplift pulse (with magnitude up to 1.5 km) between 90–70 Ma that is not observed in the paleo-water depth record. In general the amplitude of elevations predicted from the geodynamic models (up to -4 km) overestimate observed, mostly neritic, O(10) m, paleo-water depths.

3.5 Models M5–7

Models M5–M7 are based on examples presented in *Hassan et al.* (2015) and *Barnett-Moore et al.* (2017). Plumes are present in models M5–6 due to a 100 km thick, 2.5% denser basal thermochemical layer above the core-mantle boundary that is thinner than the basal thermal boundary layer (300 km). Like models M2–M4, M7 contains a 113 km basal thermochemical layer above the core-mantle boundary made of 10% denser than ambient mantle, which suppresses plume formation. All models assume a mantle adiabat, where thermal expansion is set to decrease with depth (i.e., background mantle temperature is depth-dependent). They have an initial potential temperature of 1252°C and a temperature drop of 952°C between thermal boundary layers. Viscosity variation with temperature is parameterized using Arrhenius laws. The models incorporate viscous dis-

sipation and adiabatic heating, internal radiogenic heating, and have a $Ra = 5\times10^8$. Model M5 is equivalent to model *M3* developed by *Hassan et al.* (2015) and incorporates the plate reconstruction of *Seton et al.* (2012), with modifications for the Arctic from *Shephard et al.* (2013), and modified absolute plate motions from *Shephard et al.* (2014). Model M6 uses plate reconstructions of *Müller et al.* (2016a) and *Müller et al.* (2016b) and is equivalent to model *C1* of *Barnett-Moore et al.* (2017).

Models M5–M7 have highest power at degree $l = 1$. Power drops off by more than an order of magnitude between $l = 3$ and 5. Models M5–M7 significantly under-predict the amplitude of net uplift. Nor can these models fully explain the large-scale surface tilt of the North American Western Interior. Conversely, the absolute amplitudes of models M5–M7 tend to match observed paleo-water depth within error. An important consideration is that sediment infill of accommodation space generated by dynamic drawdown could result in the maintenance of shallow paleo-water depths. This hypothesis can be investigated using the history of basement subsidence and sediment accumulation in the Western Interior Basin (e.g., Figure 6).

3.6 Summary of predicted dynamic topography and independent observations

The predictions of dynamic topography from models M1–M7 are successful at recreating the broad patterns of uplift and drawdown of the North American Western Interior. Similarly, they have been shown to agree with broad patterns of continental inundation estimated using the fossil record (*Müller et al.*, 2018). However, some substantial discrepancies between the geological record of large-scale vertical motions and predictions from geodynamic models exist. For instance, predicted dynamic topography is inconsistent with amplitudes and polarities of net post-Cretaceous vertical motions in the North American Western Interior (Figures 4-6). Similarly, predicted paleo-bathymetries of the Western Interior Basin also tend to be discrepant (Figure 4). It is intriguing that models that predict paleo-bathymetry with some fidelity tend to be poor predictors of net changes in vertical motions, and vice versa (e.g., Figure 5). As *Müller et al.* (2018) discuss, an obvious source of discrepancy between observations and model predictions is excising contributions from the lithosphere and uppermost convecting mantle (uppermost 250–350 km) from predictions of vertical motions, which is common practice in such studies (see, e.g., Section 3.1). Thus, in the rest of this paper we explore whether the discrepancies between model predictions and observations can be explained by evolution of North American upper mantle.

4 Assessing Shallow Mantle Contributions to Modern Topography

It is well known that uplift and subsidence at, or close to, Earth's surface are often dominated by the thermal and structural evolution of the lithosphere (e.g., *Watts*, 2001). Changes in asthenospheric buoyancy via thermal expansion also appear to be important contributors to observed patterns of uplift (*Parsons & Daly*, 1983; *Rudge et al.*, 2008; *Hartley et al.*, 2011; *Ghelichkhan et al.*, 2021). Surface response kernels indicate that the shallow mantle (< 400 km) exerts a key role in controlling evolution of Earth's topography (*Parsons & Daly*, 1983; *Colli et al.*, 2016; *Richards et al.*, 2020). Calculated sensitivity kernels indicate that the convecting mantle directly beneath the lithosphere-asthenosphere boundary produces the strongest contributions (from the convecting mantle) to isostatic topography (e.g., *Parsons & Daly*, 1983; *Colli et al.*, 2016; *Ghelichkhan et al.*, 2021). These results are supported by instantaneous flow models, which show, first, that topographic deflections caused by internal buoyancy anomalies have amplitudes that are inversely proportional to the depth of the anomaly (*Hager & Richards*, 1989). Secondly, they indicate that amplitudes of topography most closely approximate those expected for full isostatic compensation when they are generated by buoyancy variations in the uppermost mantle (asthenosphere and lithosphere). One of the key outstanding challenges is being able to "see through" isostatic contributions from the crust and shallow mantle to test predictions from geodynamic models of mantle convection. Here, we first summarise geophysical and geochemical observations that indicate shallow mantle contributions to the modern elevation of the North American Western Interior. Simple isostatic calculations are then used in conjunction with those insights to estimate contributions to net vertical motions of Cretaceous and younger marine rock from excess asthenospheric temperatures and changes to lithospheric structure.

4.1 Geophysical features of shallow North American mantle

Seismic shear-wave velocities (V_S) are sensitive to temperature in the upper mantle and provide a useful guide to the thermal state of the lithosphere and asthenosphere beneath continents (e.g., *Schutt & Lesher*, 2006). Figure 7A shows a slice at 125 km depth through the SL2013sv shear wave velocity model and the location of Late Cretaceous to Recent mafic magmatism (*Fitton et al.*, 1991; *Walker et al.*, 2006; *Roy et al.*, 2009; *Schaeffer & Lebedev*, 2014; *Klöcking et al.*, 2018). Shear wave velocities show a distinctive spatial pattern, being slow in the west and fast in the east, separated by an undulating boundary. Slow velocities broadly coincide with the location of Late Cretaceous to Recent magmatism, giving complimentary indications of anomalously warm asthenosphere and thin lithospheric mantle (*Ball et al.*, 2021).

To quantify the role of upper mantle temperatures in generating vertical lithospheric motions, the SLNAAFSA V_S tomography model of *Hoggard et al.* (2020)—a hybrid which embeds high-resolution regional models for North America (SL2013NA; *Schaeffer & Lebedev*, 2014), Africa (AF2019; *Celli et al.*, 2020) and the South Atlantic (SA2019; *Celli et al.*, 2020) within the global SL2013sv model of *Schaeffer & Lebedev* (2013)—is converted to temperature using the methodology of *Richards et al.* (2020). This approach incorporates recent experimental parameterisations of anelasticity at seismic frequencies (Yamauchi & Takei, 2016), allowing the highly non-linear relationship between V_S and temperature at near-solidus conditions (e.g., within the asthenosphere) to be accurately constrained. Our best-fitting anelastic parameters for this model differ slightly from those quoted in *Hoggard et al.* (2020), due to our use of an updated oceanic lithospheric cooling model (*Richards et al.*, 2020, instead of *Richards et al.*, 2018). The parameters controlling the unrelaxed shear modulus, μ_U, are μ_0=75.91 GPa, $\partial\mu/\partial T = -0.01794$, and $\partial\mu/\partial P = 2.538$ (see *Richards et al.*, 2020, their Equation 8), while those controlling the steady-state diffusion creep viscosity and proximity to the solidus are $\eta_0 = 9.538 \times 10^{22}$ Pa s, $E_a = 4.889 \times 10^5$ J mol^{-1}, $V_a = 6.26 \times 10^{-7}$ m^3 mol^{-1}, and $\partial T_s/\partial z = 0.9309$°C km^{-1} (see *Richards et al.*, 2020, their Equations 9 & 11). Note that this parameterisation is only valid in the upper 400 km of the mantle, since calibrated material properties are appropriate for an olivine-dominated composition and do not account for phase transitions. In addition, the uppermost 50 km is excluded from our analysis to avoid errors associated with downward bleeding of crustal velocities to lithospheric depths, a problem that is particularly pronounced in continental interiors and leads to unrealistically elevated temperature predictions at shallow depths.

Calculated temperatures for the 125 km depth slice are shown in Figure 7B, and other depth slices are shown in the Supporting Information (Figure S5). As expected, temperatures follow the patterns of the V_S tomography model, with hottest potential temperatures in the west beneath the Basin and Range and Colorado Plateau reaching upwards of ∼1445°C. Mantle temperature estimates can be used to map the depth to the lithosphere-asthenosphere boundary (LAB), defined here by the 1200° C isotherm (white dashed line in Figure 7B; Figure S6), which delineates a region of thinner lithosphere in the west. Note that defining the LAB by the 1300°C isotherm, as has been done in other studies (*Afonso et al.*, 2016), does not significantly change the observed thickness or location of significant gradients in thickness (white solid line in Figures 7B).

Figure 7C shows lithospheric thickness as defined by the 1200°C isotherm, filtered to include only spherical harmonic degrees smaller than $l = 60$ (wavelengths < 660 km; the unfiltered LAB is included in the Supporting Information, Figure S7). This filtering approach seeks to remove small-scale features that might be a consequence of artefacts in the underlying SLNAAFSA tomographic model. Comparison of mantle temperature and LAB depths to the observed net uplift shows that most of the uplift since the Late Cretaceous has occurred atop lithosphere that is thin compared to the interior of the continent and atop asthenosphere that is relatively warm (cf. Figures 1, 3 & 7D). The most prominent anomaly is centred on the protuberance of thicker lithosphere beneath the Colorado-Utah-Wyoming state borders, where uplift is high yet the lithosphere is thick. This region also coincides with a spatial gap in magmatism, and may indicate a more melt-depleted and viscous lithosphere.

Figure 8 shows cross-sections of topography, mantle temperatures and lithospheric thicknesses from west to east (see Figure 7B for locations). Topographic data was extracted from the SRTM90 dataset (*Jarvis et al.*, 2008). Mantle temperatures and lithospheric thicknesses were calculated in

this study (Figure 7). Crustal thicknesses were extracted from the PnUS model (*Buehler & Shearer*, 2016). Coloured circles and squares show the present-day elevation of PBDB and stratigraphic uplift constraints, respectively. They are shown atop 100 km-wide swath profiles of elevation (see *Fernandes & Roberts*, 2021). Crustal thicknesses (black dashed lines) do not exceed 50 km and show no significant variation below topographic gradients. Assuming crustal composition does not vary significantly laterally, changes in crustal thickness alone cannot be used to explain the topographic gradient (*Roberts et al.*, 2012; *Klöcking et al.*, 2018; *Levandowski et al.*, 2018). On the other hand, lithospheric and asthenospheric temperatures show significant lateral variation, and consequently so does lithospheric thickness. All cross sections show an increase in lithospheric thickness to the east, accompanied by a drop in surface elevations. The magnitude of lithospheric thickness and topographic change, however, varies significantly from north to south. Cross section X–X′, crossing the Northern Rocky Mountains, shows LAB depth increasing from ∼125 km to ∼225 km from east to west, concomitant with a change in the mean elevation of ∼1.6 km. Moving south to cross section Z–Z′, LAB depth increases from ∼80 km beneath the Southern Rocky Mountains to ∼ 200 km beneath the eastern Great Plains, accompanied by an elevation difference of ∼2.8 km. Elevations between the Colorado Plateau and the Southern Rockies also have similar changes in shallow mantle temperatures and elevations.

The correspondence between upper mantle temperatures and changes in surface elevation suggests that the uppermost mantle may have played an important role in controlling the evolution of topography in the North American Western Interior. We thus combine these geophysical observations with simple isostatic models to quantify the contributions of mantle temperature and changing lithospheric thickness to the uplift history of the North American Western Interior.

4.2 Topographic support from asthenospheric thermal anomalies

We first assess contributions to topographic support from an asthenospheric channel, h, that sits directly beneath the lithosphere (see Supporting Figure S8). Absolute asthenospheric temperatures, T, are calculated using the SLNAAFSA tomographic model and the V_S to T conversion scheme summarised in Section 4.1 (Figures 7–8). Prior to calculating support, absolute temperatures are converted into potential temperatures. We do so because absolute temperatures vary as function of depth, z, (strictly pressure), and we are interested in isolating contributions from thermal anomalies. Potential temperature, T_p is related to absolute temperature, T, such that

$$T_p = (T + 273) \exp\left(-\frac{\alpha g z}{C_p}\right) - 273, \tag{2}$$

where thermal expansivity $\alpha = 3.3 \times 10^{-5}$ K^{-1}, gravitational acceleration $g = 10$ m s^{-2}, heat capacity $C_p = 1187$ J K^{-1} kg^{-1}. Calculated temperatures are used to estimate excess potential asthenospheric temperatures, ΔT_p. They are calculated by taking the difference between the mean T_p for the layer and the background, here $T_p^\circ = 1333$°C. Support (strictly, uplift relative to reference mantle), U—assuming isostasy prevails—can then be calculated as

$$U = \frac{h \alpha \Delta T_p}{1 - \alpha T_p^\circ}. \tag{3}$$

Note that calculated support is relatively insensitive to the choice of assumed background temperature (see, e.g., *Rudge et al.*, 2008). Inspection of Equation 3 shows that support is sensitive to changing the thickness of the anomalously hot layer and excess temperature; doubling either doubles the support. We acknowledge that the thickness of the asthenospheric channel h can be defined in different ways. Mean excess temperatures for different definitions are given in the Supplementary Information (Figure S8). Estimated support for layers thicker than ∼ 100 km are likely unreliable because the isostatic approximation underpinning Equation 3 becomes less valid and predicted topography begins to significantly overestimate the true amplitude of asthenospheric contribution to dynamic topography. Table 1 summarises the sensitivity of calculated support to each parameter in Equation 3 for unit adjustments. Sensitivity of all model parameters is explored in Figure 9, which we return to later after lithospheric isostatic calculations are introduced.

We can now use stratigraphic data (Figure 3) and mantle temperatures derived from V_S tomography (Figure 7) to investigate whether the observed elevation of marine rock could be a con-

Table 1. Support (strictly uplift relative to reference mantle) from heating an asthenospheric layer beneath the lithosphere with thickness $z_L = 200$km and background (reference mantle) potential temperature $T_p^\circ = 1333°$C by 1°C.

Parameter	Reference value	δ	ΔU (km)	%
h (km)	100	±1	3.66×10^{-5}	1.01
T_p° (°C)	1333	±1	1.30×10^{-7}	3.6×10^{-3}
z_L (km)	200	±1	1.04×10^{-6}	0.029

sequence of support by asthenospheric heating. First, marine rock elevations were (spatially) averaged in $1\times1^\circ$ bins, which approximates the resolution of the shear wave tomography model. For each binned set of elevations, excess potential temperature within a 100 km thick layer beneath the base of the lithosphere was extracted from the T_p grid (Figure 7D; Supplementary Information). Binned elevations as a function of asthenospheric potential temperature are shown in Figure 10A, with the physiographic province of each measurement indicated by colour (see Figure 1B for locations and colours).The distribution of elevations is broadly uniform between 0.5 and 2 km. The distribution of potential temperatures is unimodal, with cool mantle temperatures in the shallowest 100 km beneath the lithosphere (mostly $1200 < T_p < 1300$°C), with respect to assumed background mantle temperature $T_p = 1333$°C. Few locations beneath the Colorado Plateau and Basin and Range have calculated shallow mantle potential temperature anomalies exceeding 1333°C, in agreement with estimates of potential temperatures for the region from basalt geochemistry (*Klöcking et al.*, 2018).

Equation 3 can be used to explore whether observed elevations can be explained by asthenospheric heating alone. The solid black line in Figure 10A shows support (strictly uplift, Equation 3) predicted from heating a 100 km thick asthenospheric layer located immediately beneath the lithosphere-asthenosphere boundary. The isostatic calculation predicts no more than 500 m of uplift from a layer with $T_p = 1450$°C if heating from a background mantle potential temperature of 1333°C is assumed. If the background mantle temperature is assumed to be significantly cooler, e.g., 1200°C, maximum predicted uplift is still less than 1 km. These results indicate that isostatic support from heating of even an anomalously cool asthenospheric mantle alone cannot explain the 2–3 km of observed elevations. At most, ∼1 km of uplift of the Colorado Plateau and Basin and Range can be explained by warming of initially cool asthenospheric mantle. Other obvious contributors to isostatic support are lithospheric thicknesses and densities. Thus, in the following subsection we assess the consequences of thermally equilibrated and disequilibrated lithosphere for generating observed patterns of uplift.

4.3 Relations between the lithosphere and elevation of marine stratigraphy

We examine contributions from thermally equilibrated and disequilbrated lithosphere with a view to assessing the range of topographic support that lithospheric mantle could provide to topography. We discuss their geologic implications, with regards to histories of lithospheric thinning, in Section 5. Assuming isostasy prevails, support as a function of thermally equilibrated lithospheric thinning, $U(\Delta t_L)$, is given by

$$U(\Delta t_L) = \frac{1}{\rho_a}\left[t_{L_i}(\rho_{L_i}-\rho_a) + t_{TBL_i}(\rho_{TBL_i}-\rho_a) + (t_{L_i}-\Delta t_L)(\rho_a-\rho_{L_f}) + t_{TBL_f}(\rho_a-\rho_{TBL_f})\right] \quad (4)$$

where t_{L_i} and is the initial lithospheric thickness, t_{TBL_i} and t_{TBL_f} are the initial and final thickness of the thermal boundary layer, respectively. Density of asthenospheric mantle is given by ρ_a, and the initial and final densities of lithospheric mantle and thermal boundary layer are given by ρ_{L_i}, ρ_{L_f}, ρ_{TBL_i}, ρ_{TBL_f}, respectively. The depth to the base of the thermal boundary layer, z_{TBL}, is defined as a linear function of the thickness of the lithosphere, and is given by

$$z_{TBL} = (1.678 z_{L_1}) - 5.472, \tag{5}$$

where z_{L_1} is the depth to the base of the lithosphere. This relationship is derived by analysing the correspondence between the depth to the 1200°C isotherm inferred from V_S-derived geothermal profiles and the depth to the base of the thermal boundary layer obtained by fitting steady-state geotherms to these V_S-based temperature predictions (see Text S3 and Equation S1 in *Hazzard et al.*, 2023).

In an idealised case, density of the lithospheric mantle, thermal boundary layer and asthenospheric mantle are taken to be a function of temperature. Mantle density, ρ_m, is calculated as

$$\rho_m = \rho_\circ \left(1 - \alpha \overline{T_m}\right), \tag{6}$$

where $\rho_\circ$ is the reference mantle density at standard temperature and pressure (3.33 Mg m^{-3}), α is the mantle thermal expansivity, and $\overline{T_m}$ is the average temperature of the mantle layer. For lithospheric mantle densities, ρ_L, compositional variation can be included as $(1-d)\rho_\circ(1-\alpha\overline{T_a})$ where d is a lithospheric density depletion factor between 0 and 1. The temperature of the lithospheric mantle is calculated assuming a linear geothermal gradient from the surface, here set to 0°C, to the base of the lithosphere, defined at the 1200°C isothermal surface. The temperature of the thermal boundary layer is calculated assuming an upper bounding temperature of 1200°C and a basal temperature calculated assuming an adiabatic gradient defined by Equation 2. Similarly, temperature of the asthenospheric mantle is calculated using the same adiabatic gradient.

These equations can be used to propagate uncertainties and to assess the sensitivity of calculated support to the properties of the lithosphere. Table 2 shows sensitivity of calculated support to unit adjustment, δ, of each parameter. Calculated support is most sensitive to density depletion.

To develop greater statistical insight, we performed a Monte-Carlo error analysis. One million calculations of isostatic support in response to thinning the lithosphere by 1 km, and unit adjustments to all other parameters, were performed. All parameters were varied within specified ranges and have well-defined (mostly normal) distributions (Figure 9). Crustal thickness was varied such that the mean and variance reflected values observed within the North American Western Interior (mean = 40 km, standard deviation = 10 km; *Buehler & Shearer*, 2016). Initial lithospheric thickness was also assigned a mean of 150 km and standard deviation of 30 km, reflecting the vertical resolution of the SLNAAFSA tomography model. Thermal expansion coefficient, 3.3×10^{-5}, was assigned a 10% standard deviation, which encompasses the predicted range of values as reported by *Bouhifd et al.* (1996) and *Katsura et al.* (2009). Similarly, the temperature at the base of the lithosphere, 1200°C, adiabatic gradient, simplified to 4.44°C/km, and reference mantle density, 3.33 Mg m^{-3}, were all assumed to have a standard deviation of 10%. Mantle potential temperature, 1333°C, was assigned a standard deviation of 100°C, which encompasses a range of values for 'standard' mantle (*Parsons & Sclater*, 1977). Lithospheric density depletion was assigned an exponential distribution with a length-scale of 0.005. Parameters were varied first simultaneously, shown in Figure 9A, then individually, Figure 9B–I.

The results show that there is a well-defined peak in predicted support centred at ∼24 m per km thinning, with a large uncertainty. Most of the uncertainty is a consequence of uncertain background mantle potential temperatures, thermal expansion coefficient values, temperatures at the base of the lithosphere, and mantle density depletion factors. If the density of lithospheric mantle is known, the uncertainty in predicted isostatic support is significantly reduced (see Supplementary Information). We now explore how the histories of uplift inferred from the inventory of uplifted marine rock can be used to assess the history of shallow isostatic support. We seek to quantify the roles asthenospheric temperature anomalies and changes to lithospheric architecture played in post-Cretaceous uplift of North America.

Table 2. Calculated variance of lithospheric isostatic support, ΔU, from a systematic sweep of modified parameter values (from reference values indicated in second column). Variance of parameter values, δ, are given in third column. Parameters: crustal thickness (t_{cc}, km), lithospheric density depletion factor (d), geothermal gradient ($\mathrm{d}T/\mathrm{d}z$, °C km^{-1}), mantle potential temperature (T_p, °C), temperature of thermal boundary layer (T_{bl}, °C). % indicates percentage difference to calculated support for reference lithosphere ($U = 0.03$ km). Sensitivity analysis for thinning 200 km-thick lithosphere can be found in the Supplementary Information.

Parameter	Reference value	δ	ΔU (km)	%
t_{cc}	40	± 1	1.70×10^{-4}	0.65
d	0	$+0.01$	-1.0245×10^{-2}	-39.3
$\mathrm{d}T/\mathrm{d}z$	0.44	± 0.01	5.9×10^{-5}	0.23
T_p	1333	± 1	4.7×10^{-5}	0.18
T_{bl}	100	± 1	3.2×10^{-5}	0.12

5 Exploring shallow isostatic origins for the history of observed uplift

First, we examine the consequences of assuming that lithospheric thinning alone can explain observed patterns of uplift. Thermally equilibrated lithospheric thinning requires the thermal boundary layer (between the lithosphere and convecting mantle) to be present during thinning. In contrast, thermally disequilibrated thinning implies that the thermal boundary layer is removed instantaneously during thinning and replaced by asthenospheric mantle, creating a discontinuity in temperature across the LAB. We test these two end-member scenarios to place lower and upper bounds on calculated uplift. Calculated uplift from thinning of thermally equilibrated and disequilibrated lithosphere with initial thicknesses (at 0 uplift) of 150, 200 and 250 km are shown in Figure 10B, coloured by geographic province (Equation 4). Uplift of the Great Plains and most of the Middle Rocky Mountains can be explained by thinning initially thick ($>$ 200 km) lithosphere, while uplift of the Colorado Plateau and Basin and Range can be explained by thinning of an originally relatively thin ($<$ 150 km) lithosphere.

The distribution of calculated lithospheric thicknesses are broadly bimodal (see histogram atop Figure 10B). Thus, to simplify our approach, we estimate uplift from lithospheric thinning for only these two modes. We do so by back-projecting the centroids of lithospheric thickness-uplift pairs along equilibrium and disequilibrium lithospheric thinning trajectories (Figure 10C: solid, dashed grey and black lines). The centroids were identified using a *k-means* algorithm (see Supporting Figure S9). Figure 10C-D shows the results of the *k-means* clustering algorithm. The number of clusters is chosen *a priori* by calculating the total within-cluster sum of squared distances (WCSS; see Supporting Information). The first centroid is (60 km, 1.8 km) and contains localities mostly within the Colorado Plateau, Basin and Range, and parts of the Middle and Northern Rocky Mountains. The second centroid is (170 km, 1.1 km), at the centre of a cluster encompassing localities from the Canadian shield and Interior Lowlands. Calculated initial lithospheric thicknesses for the two clusters are 130 km and 200 km. This result can be explained by thinning of lithosphere beneath the Colorado Plateau and Basin and Range from 130 km to 80–70 km. The second cluster contains loci atop lithosphere that progressively thins to the West by as much as 100 km. These results indicate that the tilting of the Great Plains, with highest uplift in the Southern and Middle Rocky Mountains, can be explained by thinning of lithosphere that was initially $\sim$ 200 km thick.

Secondly, we explore an alternative explanation in which lithosphere with different densities are thinned. Estimates of lithospheric mantle density from gravity modellingsuggests that cratonic lithosphere, present beneath the eastern region of our study area, is has a density depleted by 30–70 g cm^{-3} (*Mooney & Kaban*, 2010). Lamb et al. (2020) proposed that the lithosphere here is depleted by 20–40 g cm^{-3} compared to the asthenospheric mantle. Figure 10D shows thinning trajectories for a lithosphere that is initially 225 km thick (e.g., the modern Canadian Shield). It shows

results for different assumed reductions in density. A useful rule of thumb is that a 1% reduction lowers density by ≈ 36 kg m^{-3}. Assuming that lithospheric mantle densities were 1–2% depleted (prior to thinning) implies that up to 150 km of thinning, from an initial thickness of 250 km (across the entire domain), would be required to explain observed patterns of uplift. That would constitute a major geological event that could be tested in the future using independent observations of, for example, heat flow and xenolith-derived paleo-lithospheric thicknesses, and more granular uplift histories.

6 Discussion

There now exists a considerable body of quantitative paleogeographic, uplift and subsidence observations with which surface deflections predicted by geodynamic models of the mantle can be tested (e.g., PBDB, MacroStrat; Figures 1–3). In this study, we augmented marine fossil assemblages recorded in the PBDB with stratigraphic information to test the timing, amplitude and distribution of dynamic topography of Western North America predicted by the models presented by *Müller et al.* (2018).

Their Model M1 does not explain post-Cretaceous net uplift (it is lower by up to a factor of 2; Figure 5A). It does however broadly predict paleo-water depths that are consistent with estimates from the fossil record (Figure 5B). In contrast, models M2–M4 broadly reproduce amplitudes of net post-Cretaceous uplift (Figure 5C), but do not explain observed patterns of Cretaceous paleo-bathymetry. In particular, predicted dynamic drawdown implies a much deeper depth for the Western Interior Seaway than its fossil assemblages indicate (e.g. Figure 5D). We note that *Müller et al.* (2018)'s preferred model is M7, since it yields realistic continental flooding histories. However, the model explicitly suppresses plume formation, which probably reduces similarity to actual mantle convection. We note that calculated net dynamic topography in Model 7 is up to a factor of 3 lower than observed net uplift. Similarly, these models do not explain subsidence histories of basins in the Western Interior inferred by backstripping stratigraphy (Figure 6). As *Müller et al.* (2018) point out, an obvious source of these discrepancies is the lack of contributions to topographic support in these models from the uppermost few hundred kilometres. We addressed this issue as follows.

Recent shear wave tomographic models were used to estimate lithospheric and asthenospheric temperatures, and thence structure (Figures 7–10). This information was combined with simple isostatic calculations to assess whether shallow isostatic contributions can explain observed patterns of net uplift. Heating shallow asthenospheric mantle alone is unlikely to be sufficient for explaining observed net uplift. Maximum amplitudes predicted from heating are too low for reasonable parameter values (Figure 10A). In contrast, thinning lithospheric mantle (whether depleted or of variable initial thickness) can, on its own explain, observed patterns of uplift (Figure 10C-D). For example, petrological modelling of eclogite xenoliths from the Colorado Plateau suggest that up to 80 km shear-removal of subcontinental lithospheric mantle between Cretaceous and Eocene times, from an initial lithospheric thickness of 200 km to 120–130 km (*Hernández-Uribe & Palin*, 2019). Petrological analysis of garnet inclusions in peridotite xenoliths of the same region suggest an additional ~ 50 km of lithospheric thinning, from 130 km to ~ 80 km, from Eocene to present (*Hunter & Smith*, 1981; *Ritter & Smith*, 1996). These results are consistent with histories of sub-lithospheric support of Western North America inferred from melt histories of mafic rocks in the region (e.g., *Ball et al.*, 2021).

Figure 11 demonstrates an attempt to reconcile predicted contributions to net uplift of Western North America. They show the 'targets', i.e., net uplift estimated using fossil assemblages and associated corrections for paleo-water depth and sea-level. Also shown are estimated contributions to net uplift from the three sources considered in this paper. First, contributions from the deep mantle are extracted from *Müller et al.* (2018)'s Model M5. Secondly, isostatic asthenospheric support is estimated from excess temperatures calculated using shear wave tomography (Figure 7-8; Equation 3). Finally, the residual is attributed to lithospheric thinning, which can be compared to Figure 10. The two examples shown include a locality from the Book Cliffs in Western North America and from eastern Iowa on the Great Plains. These results emphasise the importance of constraining lithospheric thicknesses and densities for determining the history of net uplift and thus for us-

ing such observations to determine the history of mantle convection. Important future work will include refining knowledge of lithospheric densities and structure, and incorporating it into geodynamic simulations.

7 Conclusions

Histories of mantle convection and their role in generating vertical motions of Earth surface are of general interest. That a considerable body of mantle convection simulations predict differing surface defection histories indicates that identifying optimal models using independent geologic observations is likely to be a fruitful endeavour. In this paper we combine digital inventories of paleobiological data with stratigraphic information to explore origins of western North American topography. We demonstrate that geodynamic simulations that exclude the uppermost few hundred kilometres of the mantle cannot, on their own, reproduce observed patterns of vertical motions. We also demonstrate that excess asthenospheric temperatures, on their own, are insufficient for explaining net support of Western North American topography. Since crustal thicknesses across this region appear to be broadly similar we instead, turn to modification of lithospheric mantle as a source of post-Cretaceous net uplift. We demonstrate that changes to lithospheric thickness and depletion could explain observed patterns of uplift. These results emphasise the importance of determining the properties (e.g., densities and structure) of the lithosphere (especially the lithospheric mantle) and its modification by the convecting mantle if we are to understand how the convecting mantle impacts surface processes and vice versa.

8 Open Research

All data used in this publication are accessible through online, open-access data repositories. Dynamic topography models from *Müller et al.* (2018) can be accessed through the open data repository https://www.earthbyte.org/global-dynamic-topography-models/. Database for uplift measurements from paleobiological data, from *Fernandes & Roberts* (2021), can be accessed through the open data repository https://doi.org/10.1130/GSAB.S.12939470. All other datasets used in this research can be accessed in the data repository https://zenodo.org/records/10212951.

Figures

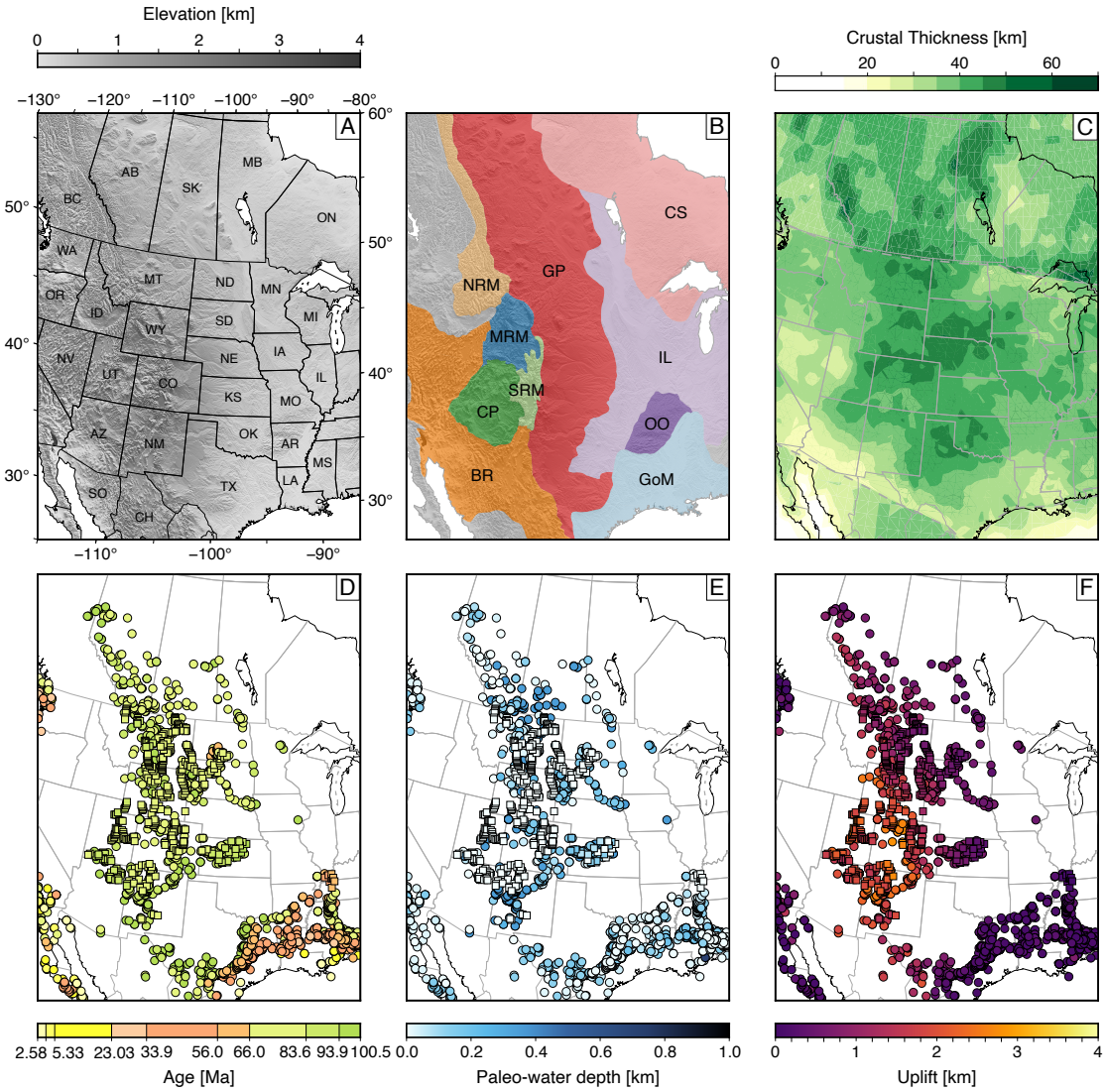

Figure 1. Western North America and its surroundings. (A) Hill-shaded elevation map showing USA, Canadian and Mexican state borders, note two-letter state abbreviations (SRTM+; *Becker et al.*, 2009). (B) Physiographic provinces after *Fenneman* (1928): CS = Canadian Shield; GP = Great Plains; NRM, MRM, SRM = Northern, Middle and Southern Rocky Mountains; CP = Colorado Plateau; BR = Basin and Range; IL = Interior Lowlands; OO = Ozark and Ouachita Mountains; GoM = Gulf of Mexico Coastal Plain. (C) Crustal thickness from CRUST1 (*Laske et al.*, 2013) and PnUS (*Buehler & Shearer*, 2016). Dashed gray lines = extent of PnUS model. (D) Location of fossil assemblages from the Paleobiology Database (PBDB; circles) indicating youngest outcropping marine to terrestrial (MTT; squares) stratigraphic transitions (*Fernandes et al.*, 2019; *Fernandes & Roberts*, 2021). Points are coloured by stratigraphic age, using the *Gradstein et al.* (2012) timescale. (E) Interpreted paleo-water depth for each location. (F) Net uplift calculated from fossil and stratigraphic data.

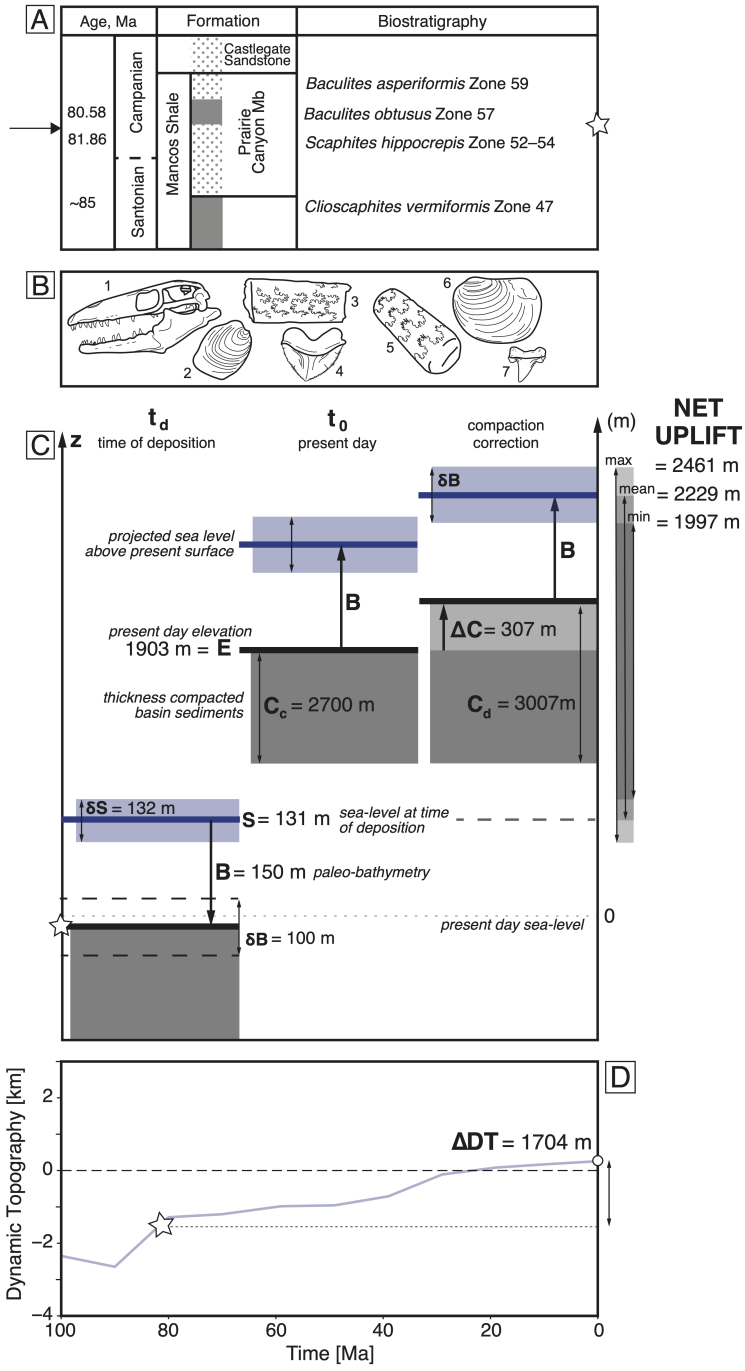

Figure 2. Illustration of methodologies used to extract observed and predicted net uplift from geological data and predictions from mantle convection simulations. Loci of the fossil assemblage in the Book Cliffs of Utah and dynamic topographic prediction is labelled '3' in Figure 3. (A) General stratigraphic framework of the Mancos Shale, and associated bio- and chrono-stratigraphic constraints. (B) Fossil assemblage used to constrain the paleo-bathymetry of the Prairie Canyon Member of the Mancos Shale: 1–Prognathodon, 2–Platyceramus cycloides, 3–Baculites haresi, 4–Squalicorax pristodontus, 5–Baculites aquilaensis, 6–Innoceramus balticus, 7–Cretolamna (see *Fernandes & Roberts*, 2021, for more details). (C) Schematic showing net uplift calculation and corrections. (D) History of dynamic topography from Model M2 of *Müller et al.* (2018) at the location of the fossil assemblage. The star marks the age of deposition of the fossil assemblage. Net predicted dynamic topography, ΔDT, is calculated as the difference between predicted dynamic topography at the time of deposition and the present-day.

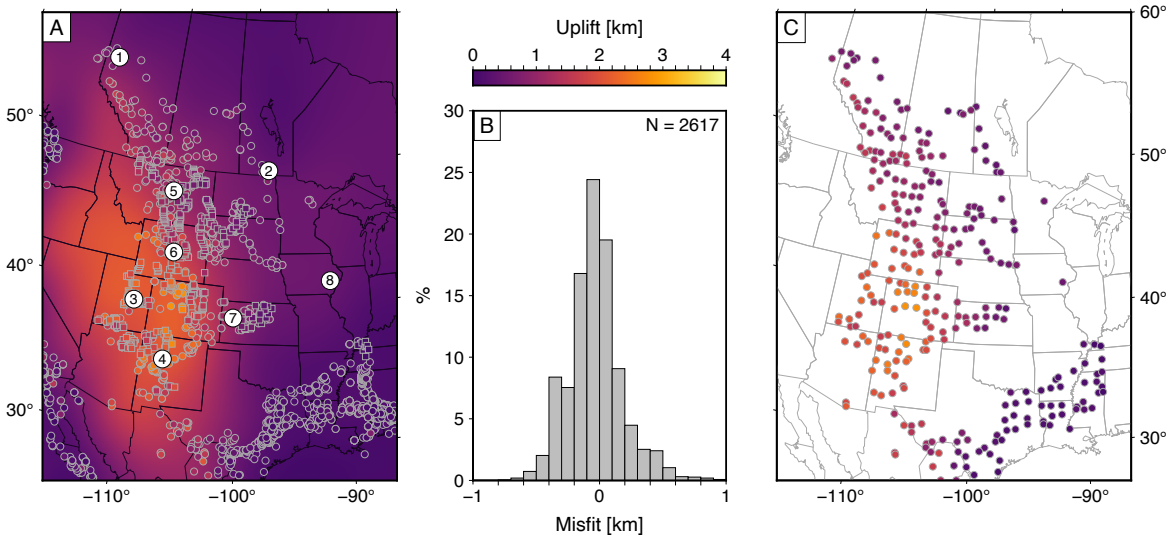

Figure 3. Large-scale patterns of uplift. (A) Smooth surface fit to 2617 spot measurements of uplift derived from the PBDB (circles) and marine to terrestrial stratigraphic transitions (squares). Large numbered circles = localities where stratigraphic observations of vertical motion and predicted dynamic topography are shown in Figure 4D and Supplementary Information. Surface was generated using continuous curvature splines and then filtered to remove wavelengths < 1000 km. (B) Difference between uplift estimated from 2617 stratigraphic (PBDB) observations and the smooth surface shown in panel A. (C) Location and mean uplift value for uplift data averaged into 1°×1° bins (N = 295). Data from the westernmost edge of the North American continent were not included as their uplift history most likely does not reflect a history of mantle-driven vertical motions.

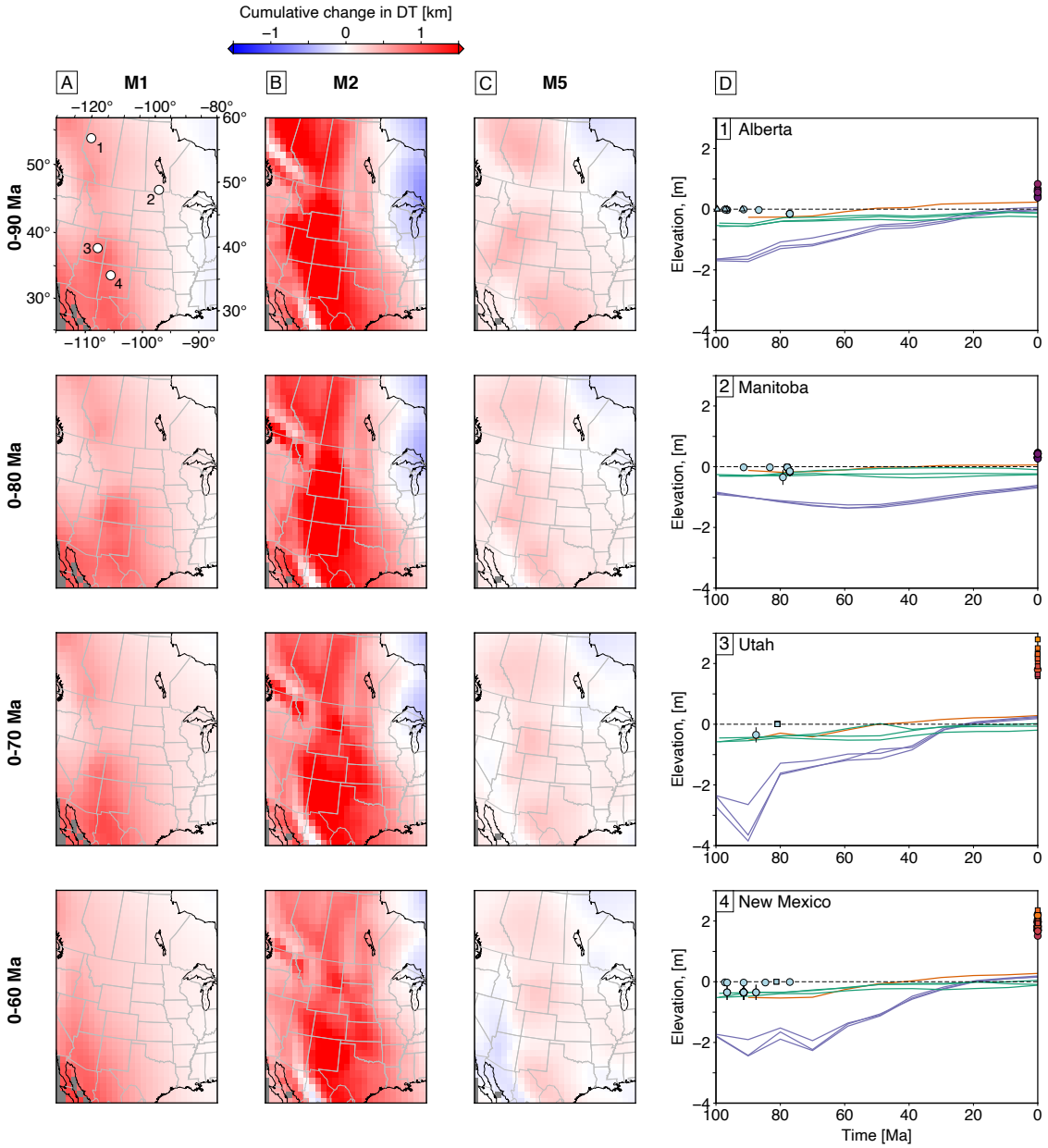

Figure 4. Comparison of dynamic topography predicted from mantle convection simulations and stratigraphic observations. Maps show cumulative change in dynamic topography since 90, 80, 70 and 60 Ma predicted by models (A) M1, (B) M2 and (C) M5, which are representative histories produced by families of models generated by *Müller et al.* (2018). Gray lines = state/country boundaries (see Figure 1A). Labelled white circles = locations of stratigraphic constraints and predicted dynamic topography shown in panel D: Alberta (1), Manitoba (2), Utah (3), New Mexico (4). (D) Histories of vertical motion predicted by geodynamic models compared to stratigraphic observations at localities labelled 1–4 in panel A. Orange, purple, green lines = predicted dynamic topography from models M1, M2–M4, M5–M7, respectively (*Müller et al.*, 2018). Circles and squares = stratigraphic observations from PBDB and first recorded terrestrial sediments, respectively, and modern topography; error bars = paleo-water depth uncertainties (colours indicate paleo-water depth, see Figure 1E; see body text for details).

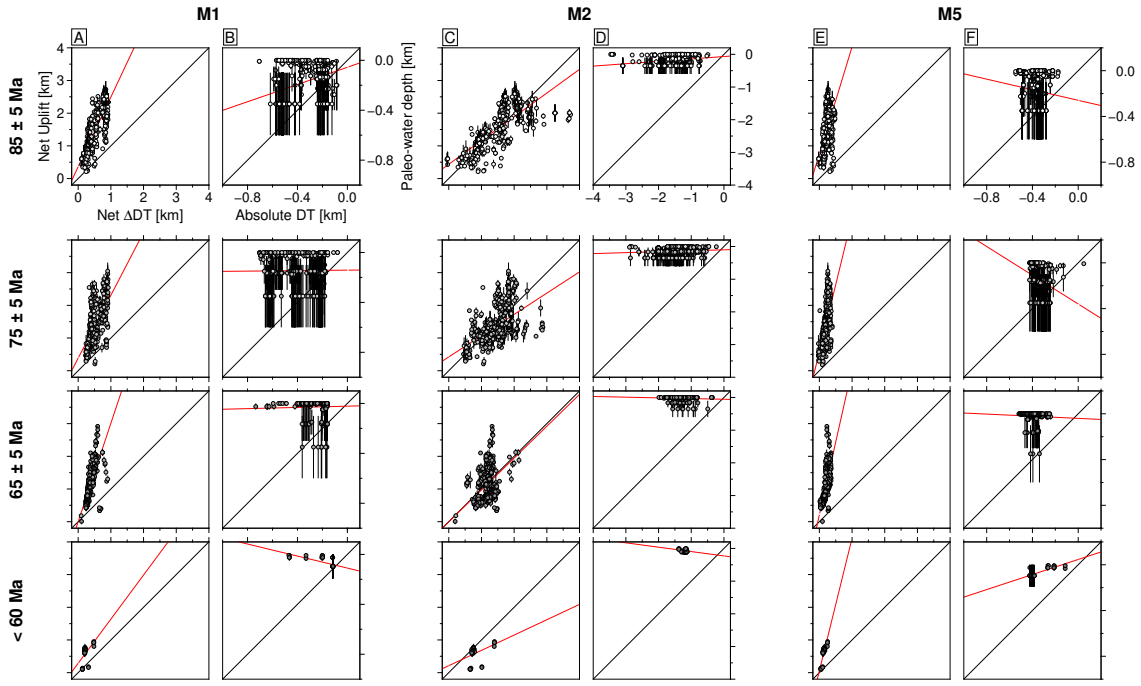

Figure 5. Comparisons of net (post-deposition) uplift and paleo-water depths from stratigraphic observations to geodynamic model predictions. (A) Circles = net uplift measured using modern elevation of marine rock compared to net change in predicted dynamic topography (see e.g. Figure 2). Measurements of net uplift are grouped according to age of deposition in 85 ± 5 Ma (top row), 75 ± 5 Ma, 65 ± 5 Ma and < 60 Ma (bottom row) bins (see Figures 1F & 2). Predictions of net dynamic topography (ΔDT) are from model M1 of *Müller et al.* (2018). Measured and predicted motions were averaged in the same 1° × 1° bins prior to insertion into this panel (see Figure 2); error bars = 1 standard deviation from the mean vertical stratigraphic motions within each 1×1° bin, which includes age and paleo-water depth uncertainties and the range of values in each bin. Black line = 1:1 relationship; red line = best-fit linear least-squares regression. (B) Comparison of predicted absolute elevations from model M1 and paleo-water depth estimates from stratigraphy in labelled age bins. (C-D) Model M2. (E-F) Model M5. See Figure 3.

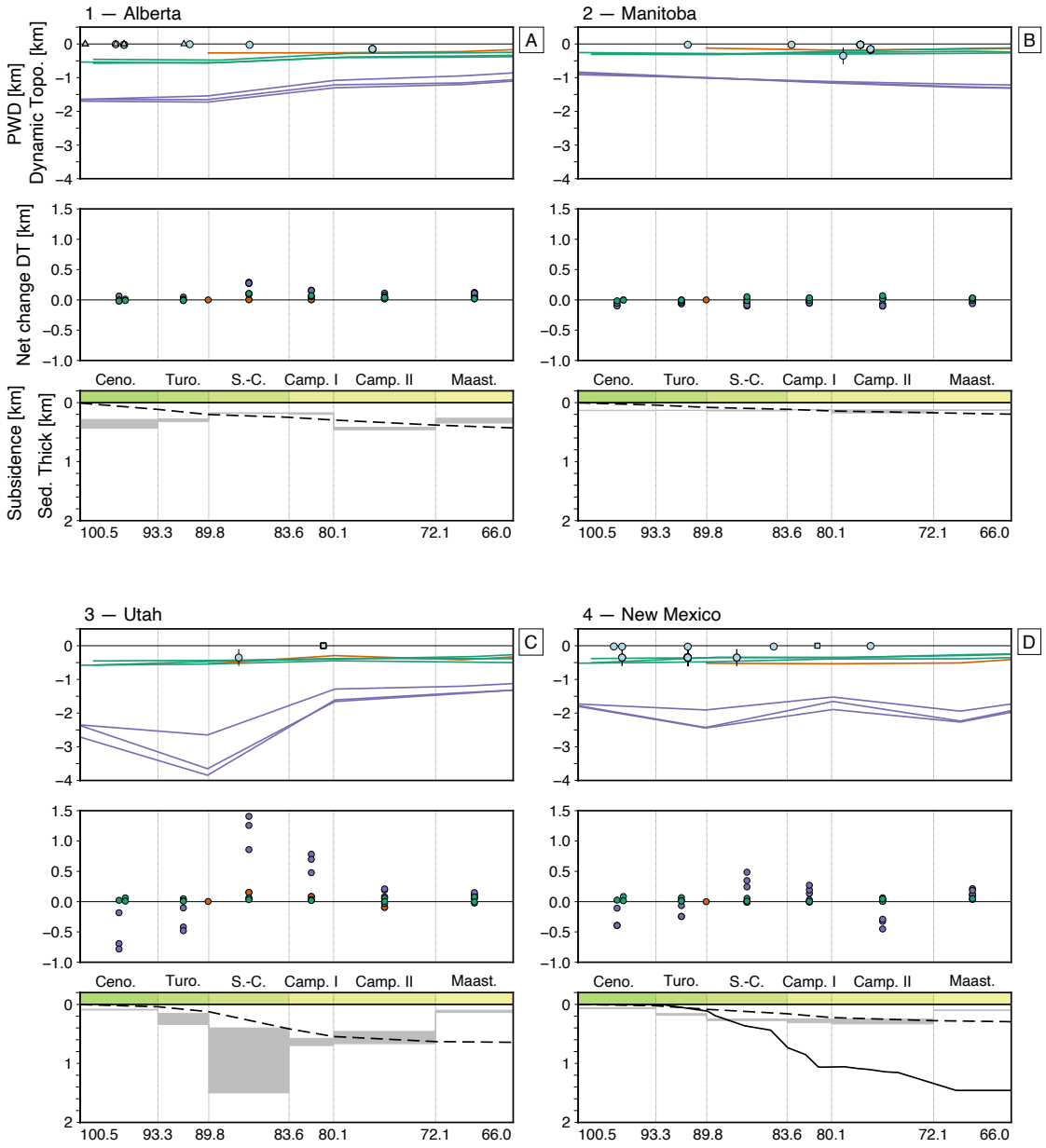

Figure 6. Comparison of predicted Late Cretaceous dynamic topography and independent subsidence histories. (A) Observations and predictions from bin (width = 30 km) centred on circle labelled 1 in Figure 2 (Alberta). Top panel: Orange, purple, green lines = predicted dynamic topography from models M1, M2–M4, M5–M7, respectively (*Müller et al.*, 2018). Circles = paleo-water depths from biostratigraphic observations; error bars = associated uncertainties, note that in many cases uncertainty is less than symbol size. Triangles = minimum paleo-water depth from marine biostratigraphic constraints where paleo-environment is poorly constrained. Squares = first recorded post-marine terrestrial sediments (*Fernandes et al.*, 2019). Vertical lines bound geological stages. Middle panel: Net change in predicted dynamic topography during each stage for the seven mantle convective simulations (colours as for lines in panel A); Ceno = Cenomanian, Turo = Turonian, S-C = Coniacian-Santonian, Camp I & Camp II = Campanian, Maast = Maastrichtian. Negative/positive values indicate predicted net subsidence/uplift. Bottom panel: Black dashed line = subsidence history from backstripping, decompacting and air-loading isopach maps from *Roberts & Kirschbaum* (1995), see Supplementary Information. Grey bands = sediment thickness within bin for each stage, also from *Roberts & Kirschbaum* (1995). (B) Manitoba (centred on circle labelled 2 in Figure 2A). (C) Utah (3). (D) New Mexico (4). Black solid line is air-loaded subsidence curve from Well 3 (−110.178°, 39.435°) presented in *Liu et al.* (2014).

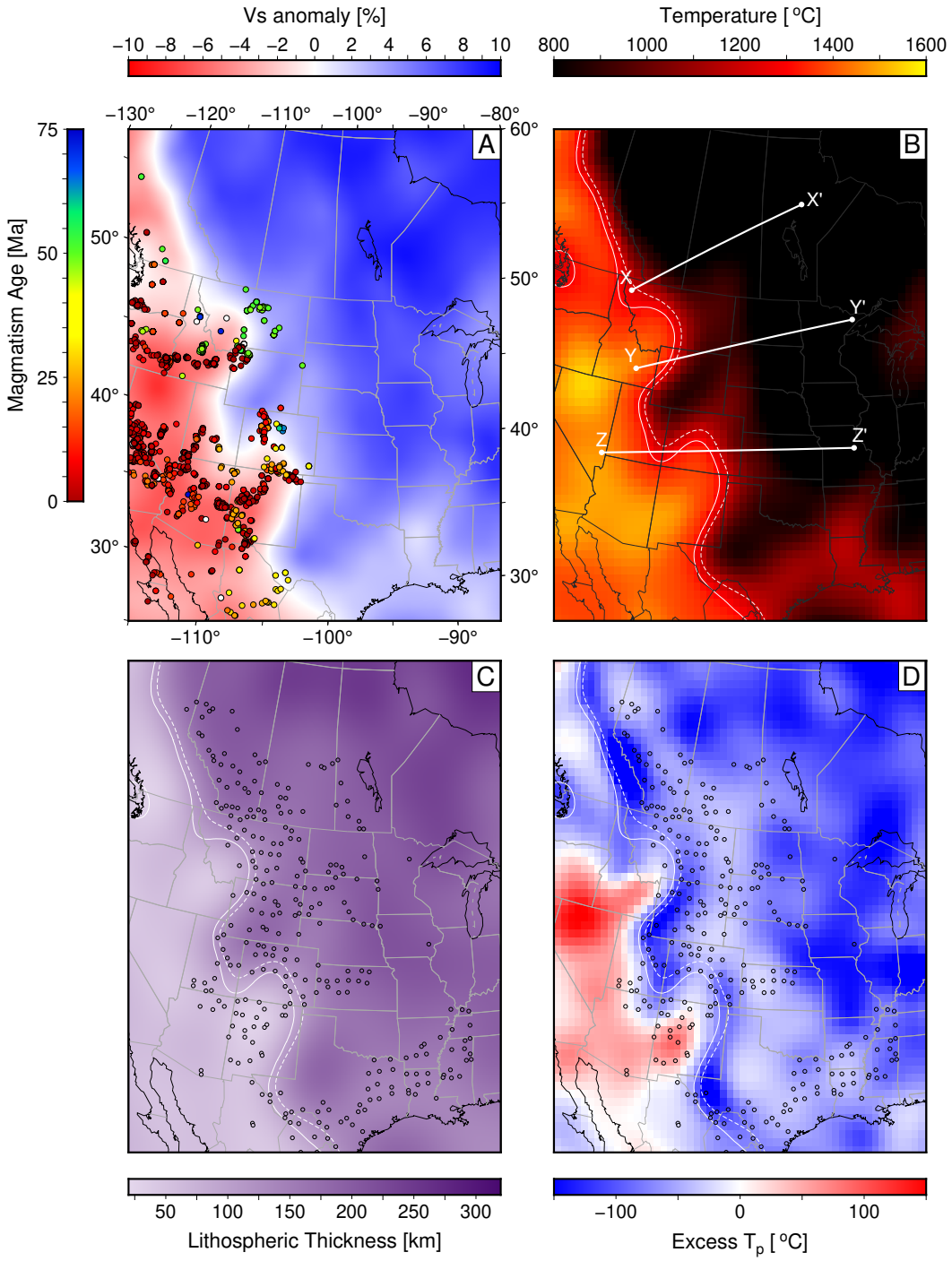

Figure 7. Shallow mantle geometries, mafic magmatism and uplift constraints. (A) Shear wave velocity anomaly at 125 km depth from *Schaeffer & Lebedev* (2013). Circles = magmatism coloured by age from NAVDAT database with MgO > 4 wt% (*Walker et al.*, 2006). Gray lines = state/country boundaries. (B) Temperature at 125 km estimated from conversion of *Schaeffer & Lebedev* (2014)'s shear wave tomography model into temperature (see body text for details). White contours = 1200°C (dashed) and 1300°C (solid) isotherms. Labelled white lines = location of cross sections shown in Figure 8. (C) Lithospheric thickness (defined by 1200°C isotherm), filtered to include spherical harmonic degrees less than $l = 60$ (wavelengths > 660 km). Black circles = foci of binned (1×1°) uplift measurements (see Figure 1). (D) Excess potential temperature of shallowest 100 km beneath the base of the lithosphere. White curves = temperature contours shown in panel B.

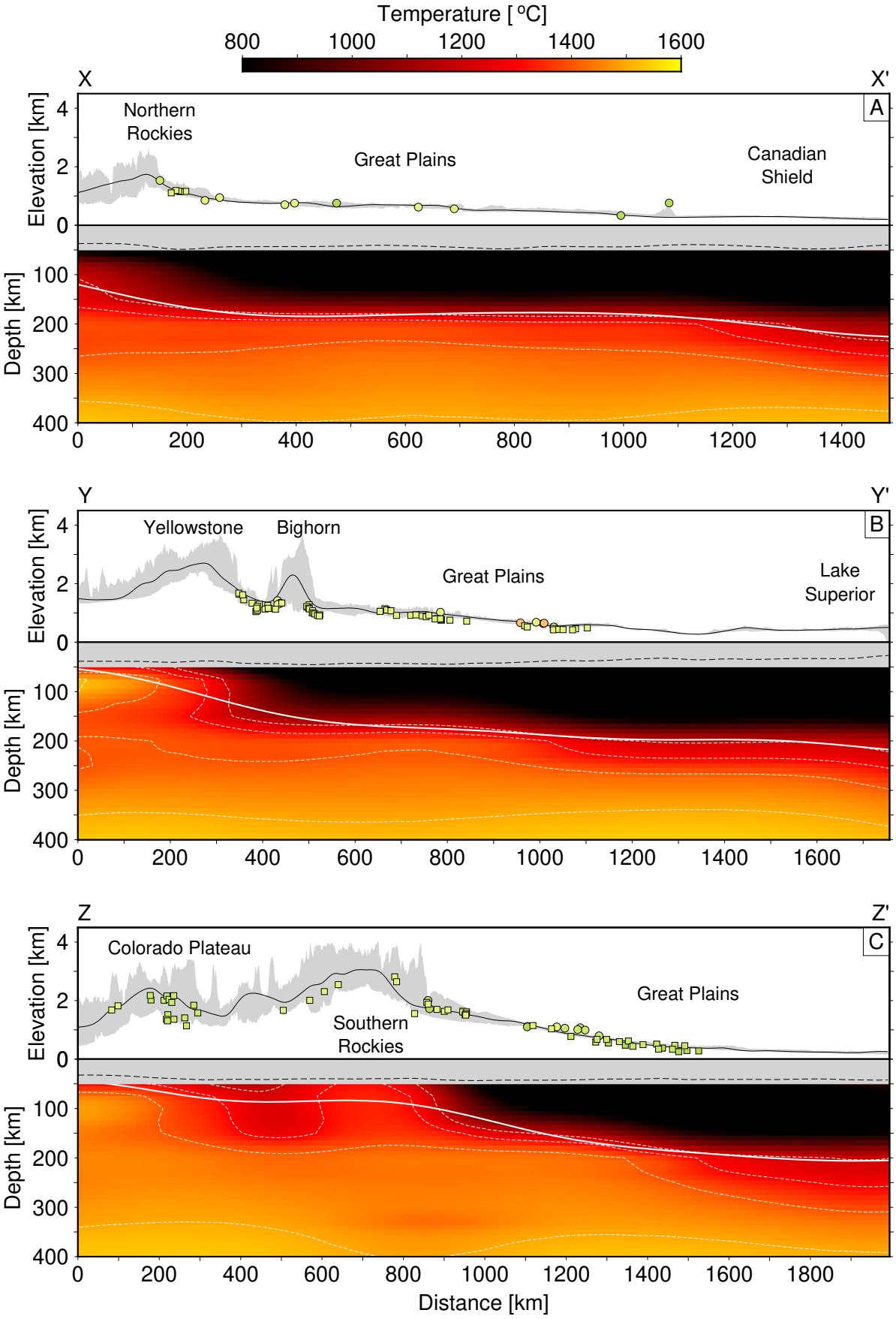
Temperature [ºC]
800
1000
1200
1400
1600
X
X'
A
Northern
Rockies
Great Plains
Canadian
Shield
Elevation [km]
Depth [km]
Y
Y'
B
Yellowstone
Bighorn
Great Plains
Lake
Superior
Z
Z'
C
Colorado Plateau
Great Plains
Southern
Rockies
Distance [km]

Figure 8. Cross sections through North American surface observations and calculated shallow mantle temperatures. (A) Top panel: Black curve = smoothed topography (100 km Gaussian low-pass filter) from Northern Rockies, through the Great Plains to the Canadian Shield (see line labelled X–X′ in Figure 6B; (SRTM90: *Jarvis et al.*, 2008). Gray band = maximum and minimum topography within 100 km wide swath. Circles = uplifted marine rocks from PBDB inventory; squares = youngest recorded marine to terrestrial transitional stratigraphy; all samples are from within 100 km wide swath and are coloured by age (see Figure 1). Bottom panel: Colours = temperatures calculated by converting a version of *Schaeffer & Lebedev* (2014)'s shear wave model (see body text for details). Thin dotted lines = isotherms in 100°C intervals. Temperatures at depths shallower than 50 km (grey band) are not shown. Black dashed line = crustal thickness from PnUS (*Buehler & Shearer*, 2016). Solid white line = lithosphere-asthenosphere boundary calculated from the 1200°C isotherm smoothed by only including scales less than spherical harmonic degree $l = 60$ (wavelengths $>$ 660 km). (B-C) Cross sections through Yellowstone to Lake Superior (Y–Y′), and Colorado Plateau to the Great Plains (Z–Z′; see Figure 6B).

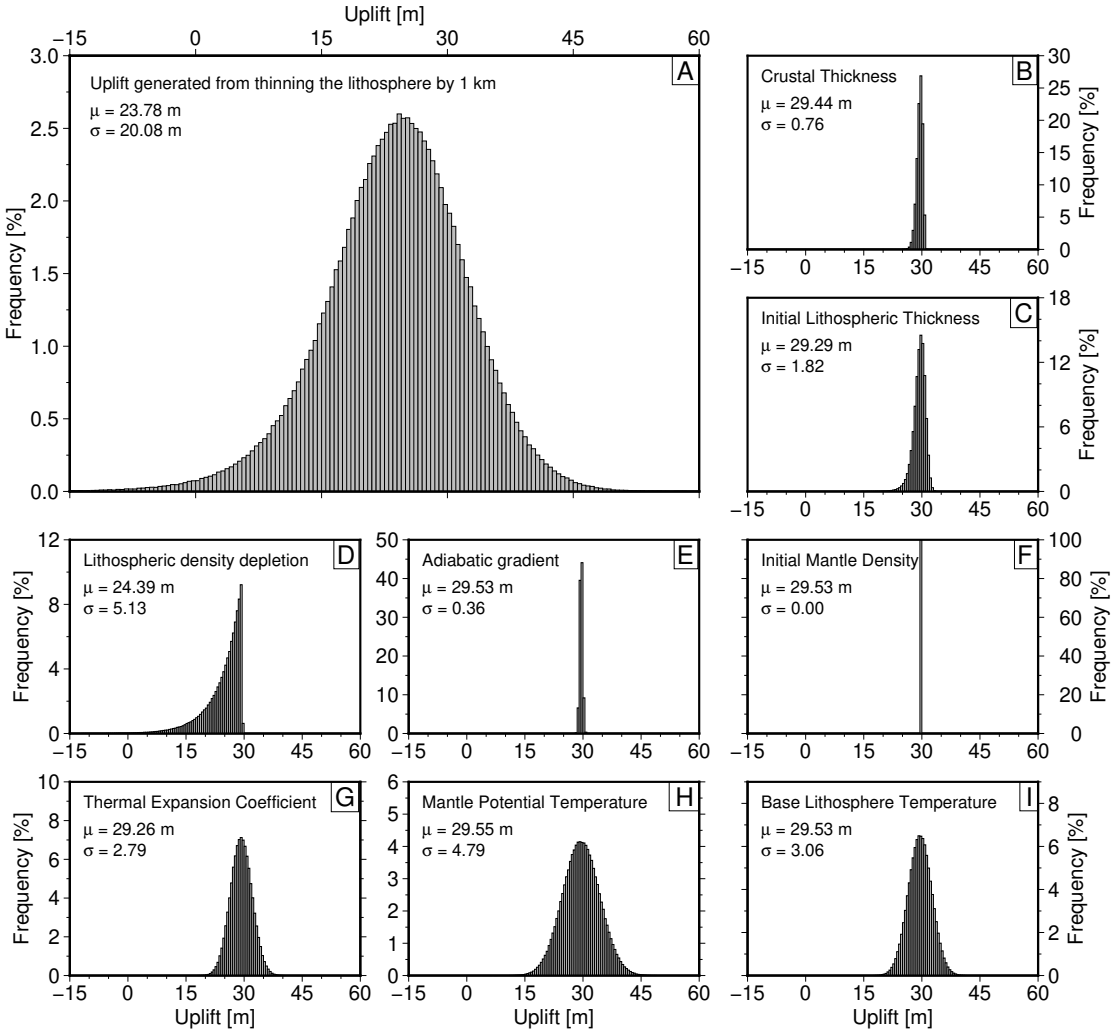

Figure 9. Sensitivity of calculated uplift to unit lithospheric thinning and other unit modifications. (A) Distribution (mean = μ, standard deviation = σ) of calculated isostatic uplift generated by Monte Carlo simulation incorporating variance of all parameters in Equation 4: crustal thickness, initial lithospheric thickness, lithospheric density depletion, adiabatic gradient, initial mantle density, thermal expansion coefficient, mantle potential temperature and temperature at the base of the lithospheric mantle. Variance of parameters included in this test are indicated in following panels. (B)–(I) Calculated distributions of uplift that arise from varying only parameters annotated in each panel.

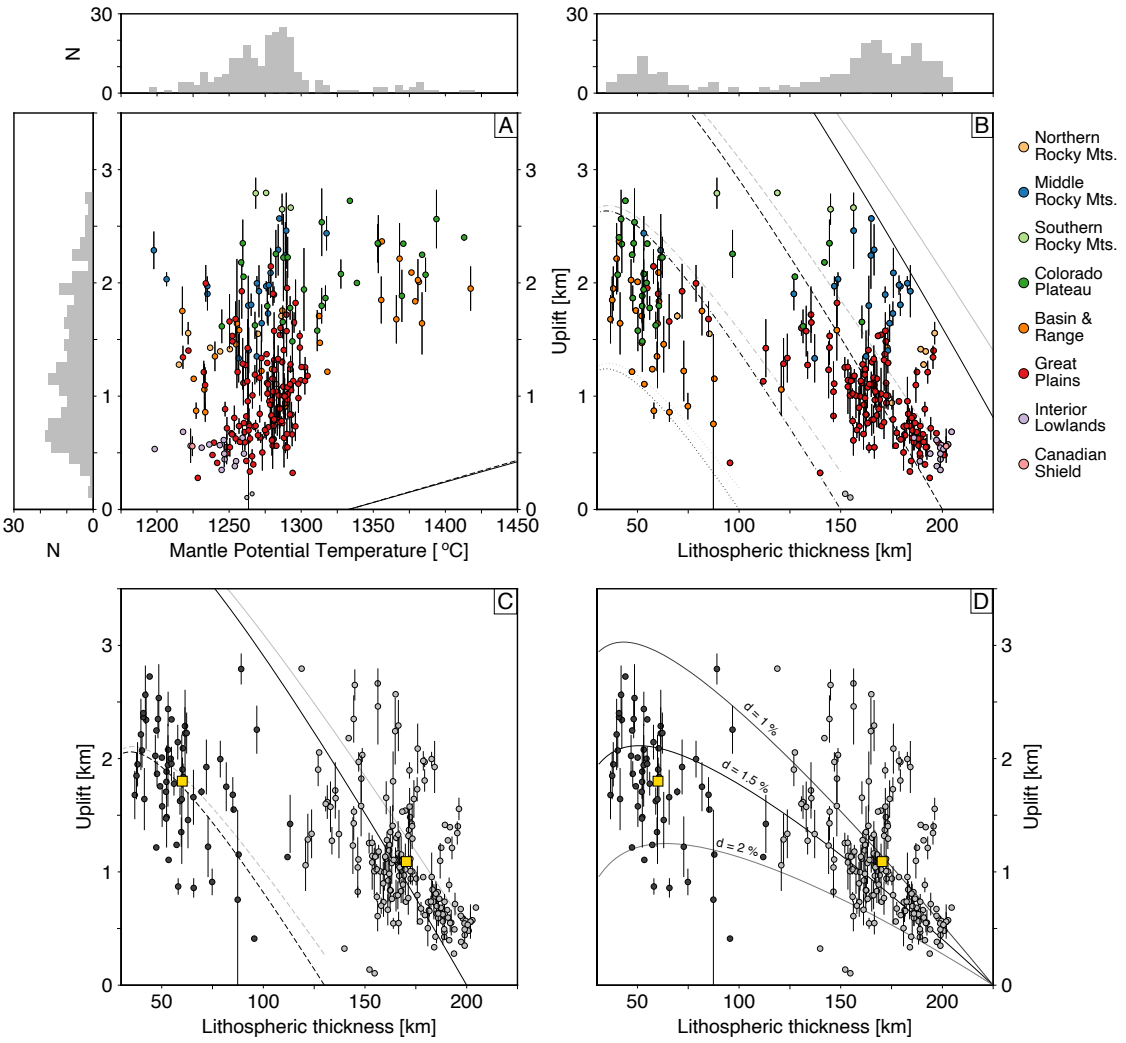

Figure 10. Assessing the role of lithospheric thinning and asthenospheric temperatures for generating observed uplift. (A) Uplift measured from stratigraphic observations compared to calculated mean potential temperatures of a 100 km thick asthenospheric channel beneath the base of the lithosphere. Circles = mean values in 1×1° bins; error bars = 1σ of uplift measurements in bin. Potential temperatures were extracted from thermal model shown in Figures 6–7 (see body text for details). Circles are coloured according to location (see legend); post-Cretaceous uplift data from the Gulf of Mexico coastal plain are not included. Histograms atop and aside main panel show distributions of calculated potential temperatures and uplift measurements, respectively. Lines = predicted isostatic uplift for anomalously warm 100 km (solid) or 200 km (dashed) thick asthenospheric channels (see body text). (B) Uplift measurements in 1×1° bins compared to lithospheric thickness estimates shown in Figure 6C. Black lines = predicted uplift for thermally equilibrated thinning of lithosphere with initial thicknesses of 250 (solid), 200 (dashed), 150 (dot-dashed) or 100 (dotted) km. Nearby gray lines are for thinning without thermal equilibration. (C) Uplift as a function of lithospheric thickness, coloured by cluster calculated using k-means clustering algorithm. Yellow squares = cluster centroids. Centroid values are consistent with (thermally equilibrated or disequilibrated) thinning of lithosphere with initial thicknesses of 130 km (black and grey dotted lines) or 200 km (back and grey dashed lines). (D) Black lines show thermally equilibrated thinning of lithosphere with initial thickness of 225 km with different degrees of lithospheric density depletion.

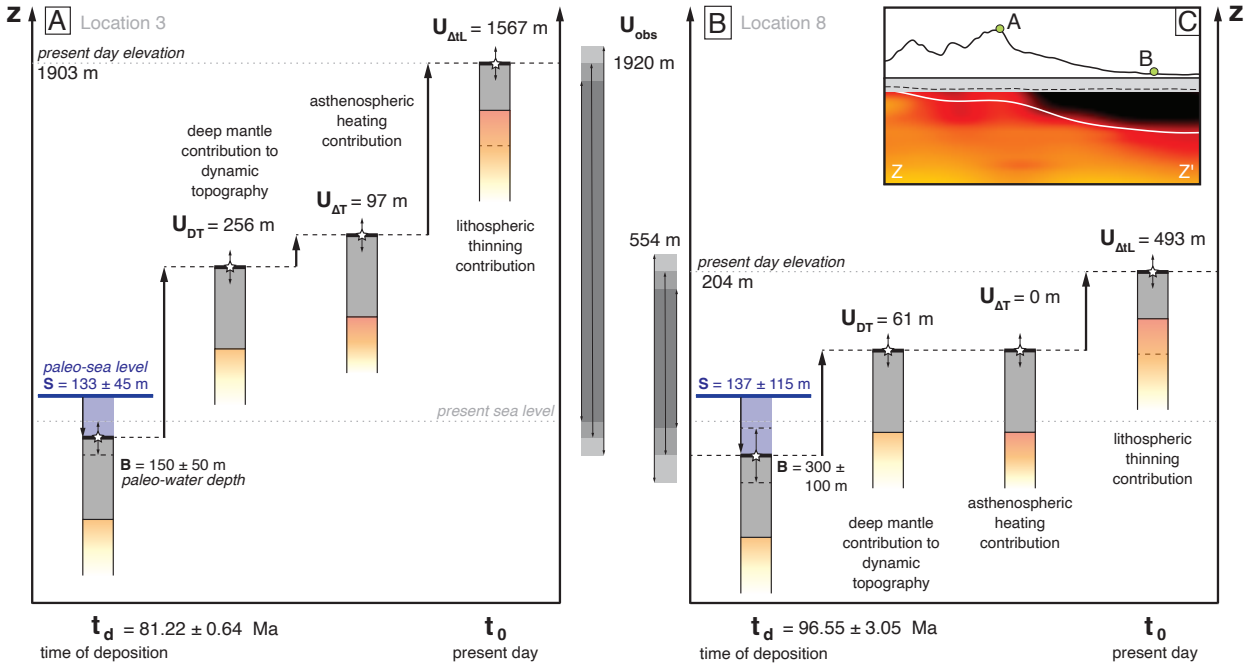

Figure 11. Reconciling dynamic and isostatic drivers of uplift in the North American Western Interior. These schematics incorporate dynamic topography predicted by mantle convection simulations (Model M5; Figure 4), and estimated additional asthenospheric heating and lithospheric thinning required to generate observed uplift (see Figure 10 and body text for details). (A) Uplift of the Book Cliffs (Location 3: Figures 2 & 3). Note that the lithospheric thinning required to match observed uplift is significantly less if predictions from models M2–M4 are considered. (B) Uplift in eastern Iowa (Location 8: Figure 3). (C) Schematic cross section across the study region showing the positions of these examples (see Figure 7B: Z–Z′ for location).

References

Afonso, J.C., Moorkamp, M. and Fullea, J. (2016). Imaging the Lithosphere and Upper Mantle *in* Moorkamp, M., Lelièvre, P.G., Linde, N., and Khan, A. (eds.) *Integrated Imaging of the Earth; Geophysical Monograph Series*. doi: 10.1002/9781118929063.ch10.

Athy, L.F. (1930). Density, porosity, and compaction of sedimentary rocks. *AAPG Bulletin*, *14*1, 1-24, doi:10.1306/3D93289E-16B1-11D7-8645000102C1865D.

Audet, P. (2014). Toward mapping the effective elastic thickness of planetary lithospheres from a spherical wavelet analysis of gravity and topography. *Physics of the Earth and Planetary Interiors*, *226*, 48-82, doi:10.1016/j.pepi.2013.09.011.

Austermann, J., Pollard, D., Mitrovica, J.X., Moucha, R., Forte, A.M., DeConto, R.M., Rowley, D.B. and Raymo, M.E. (2015). The impact of dynamic topography change on Antarctic ice sheet stability during the mid-Pliocene warm period. *Geology*, 43(10), 927-930, doi:10.1130/G36988.1.

Austermann, J., Mitrovica, J.X., Huybers, P. and Rovere, A. (2017). Detection of a dynamic topography signal in last interglacial sea-level records. *Science Advances*, *3*(7), p.e1700457, doi:10.1126/sciadv.1700457.

Ball, P. W., White, N. J., Maclennan, J. and Stephenson, S. N. (2021). Global influence of mantle temperature and plate thickness on intraplate volcanism. *Nat. Commun.*, *12*(2045), doi:10.1038/s41467-021-22323-9.

Barnett-Moore, N., Hassan, R., Müller, R. D., Williams, S. E., and Flament, N. (2017). Dynamic topography and eustasy controlled the paleogeographic evolution of northern Africa since the mid-Cretaceous. *Tectonics*, *36*(5), 929-944, doi:10.1002/2016TC004280.

Becker, J.J., Sandwell, D.T., Smith, W.H.F., Braud, J., Binder, B., Depner, J., Fabre, D., Factor, J., Ingalls, S., Kim, S-H., Ladner, R., Marks, K., Nelson, S., Pharaoh, A., Sharman, G., Trimmer, R., vonRosenburg, J., Wallace, G., and Weatherall., P. (2009). Global Bathymetry and Elevation Data at 30 Arc Seconds Resolution: SRTM30_PLUS. revised for *Marine Geodesy*, *32*(4), 355-371, doi:10.1080/01490410903297766.

Bessin, P., Guillocheau, F., Robin, C., Braun, J., Bauer, H., and Schroetter, J.-M. (2017). Quantification of vertical movement of low elevation topography combining a new compilation of global sea-level curves and scattered marine deposits (Armorican Massif, western France). *Earth and Planetary Science Letters*, *470*, 25-36, doi:10.1016/j.epsl.2017.04.018.

Blum, M., and Pecha, M. (2014). Mid-Cretaceous to Paleocene North American drainage reorganization from detrital zircons. *Geology*, *42*(7), 607-610, doi:10.1130/G35513.1.

Bond, G. (1976). Evidence for continental subsidence in North America during the Late Cretaceous global submergence. *Geology*, *4*, 557-560, doi:10.1130/0091-7613(1976)4<557:EFCSIN>2.0.CO;2.

Bouhifd, M. A., Andrault, D., Fiquet, G., and Richet, P. (1996). Thermal expansion of forsterite up to the melting point. *Geophysical Research Letters*, *23*(10), 1143-1146, doi:10.1029/96GL01118.

Buehler J.S. and Shearer, P.M. (2016). Uppermost mantle seismic velocity structure beneath USArray. *Journal of Geophysical Research*, *121*, doi:10.1002/2016JB013265.

Bunge, H. P., and Baumgardner, J. R. (1995). Mantle convection modeling on parallel virtual machines. *Computers in physics*, *9*(2), 207-215, doi:10.1063/1.168525.

Celli, N. L., Lebedev, S., Schaeffer, A. J., and Gaina, C. (2020). African cratonic lithosphere carved by mantle plumes. *Nature communications*, *11*(1), 1-10, doi:10.1038/s41467-019-13871-2.

Celli, N. L., Lebedev, S., Schaeffer, A. J., Ravenna, M., and Gaina, C. (2020). The upper mantle beneath the South Atlantic Ocean, South America and Africa from waveform tomography with massive data sets. *Geophysical Journal International*, *221*(1), 178-204, doi:10.1093/gji/ggz574.

Chamberlain, C.P., Mix, H.T., Mulch, A., Hren, M.T., Kent-Corson, M.L., Davis, S.J., Horton, T.W., and Graham, S.A. (2012). The Cenozoic climatic and topographic evolution of the western north American Cordillera. *American Journal of Science*, *312*(2), 213-262, doi:10.2475/02.2012.05.

Cobban, W.A., Walaszczyk, I., Obradovich, J.D., and McKinney, K.C. (2006). A USGS zonal table for the Upper Cretaceous Middle Cenomanian–Maastrichtian of the Western Interior of the United States based on Ammonites, Inoceramids, and Radiometric ages. *Technical report.*

Colli, L., Ghelichkhan, S., and Bunge, H.P. (2016). On the ratio of dynamic topography and gravity anomalies in a dynamic Earth. *Geophysical Research Letters*, *43*(6), 2510-2516, doi:10.1002/2016GL067929.

Conway-Jones, B. W. and White, N. (2022). Paleogene buried landscapes and climatic aberrations triggered by mantle plume activity. *Earth and Planetary Science Letters*, *593*, 117644, doi:10.1016/j.epsl.2022.117644.

Cox, K. G. (1989). The role of mantle plumes in the development of continental drainage patterns. *Nature*, *342*873-877, doi:10.1038/342873a0.

Craig, C. H., and McKenzie, D. (1987). Surface deformation, gravity and the geoid from a three-dimensional convection model at low Rayleigh numbers. *Earth and Planetary Science Letters*, 83(1-4), 123-136, doi:10.1016/0012-821X(87)90056-2.

Cross, T.A. (1986). Tectonic Controls of Foreland Basin Subsidence and Laramide Style Deformation, Western United States, in *Foreland Basins*, P.A. Allen and P. Homewood (eds.), doi:10.1002/9781444303810.ch1.

Cross, T.A., and Piliger, R.H. (1978). Tectonic controls of late Cretaceous sedimentation, western interior, USA. *Nature*, *247*, 653-657, doi:10.1038/274653a0.

Crough, S. T. (1983). Hotspot swells.*Annual Review of Earth and Planetary Sciences*, *11*, 165-93.

Czarnota, K., Roberts, G. G., White, N. J. and Fishwick, S. (2014). Spatial and temporal patterns of Australian dynamic topography from River Profile Modeling. *Journal of Geophysical Research: Solid Earth*, *119*(2), 1384-1424, doi:10.1002/2013JB010436.

Davies, D. R., Ghelichkhan, S., Hoggard, M. J., Valentine, A. P., and Richards, F. D. (2023). Observations and models of dynamic topography: Current status and future directions. *Dynamics of Plate Tectonics and Mantle Convection*, 223-269, doi:10.1016/B978-0-323-85733-8.00017-2.

DeCelles, P. G. (1994). Late Cretaceous-Paleocene synorogenic sedimentation and kinematic history of the Sevier thrust belt, northeast Utah and southwest Wyoming. *GSA Bulletin*, *106*(1), 32-56, doi:10.1130/0016-7606(1994)106<0032:LCPSSA>2.3.CO;2.

DeCelles, P. G. (2004), Late Jurassic to Eocene evolution of the Cordilleran thrust belt and foreland basin system, Western U.S.A.. *American Journal of Science*, *304*(February), 105-168, doi:10.2475/ajs.304.2.105.

Dickinson, W.R. (2004). Evolution of the North American Cordillera. *Annual Review of Earth and Planetary Science*, *32*(1), 13-45, doi:10.1146/annurev.earth.32.101802.120257.

Dickinson, W. R., Klute, M. A., Hayes, M. J., Janecke, S. U., Lundin, E. R., McKittrick, M. A., and Olivares, M. D. (1988). Paleogeographic and paleotectonic setting of Laramide sedimentary basins in the central Rocky Mountain region. *GSA Bulletin*, *100*(7), 1023-1039, doi:10.1130/0016-7606(1988)100<1023:PAPSOL>2.3.CO;2.

Ding, X., Dávila, F. M., and Lithgow-Bertelloni, C. (2023). Mechanisms of subsidence and uplift of Southern Patagonia and offshore basins during slab window formation. *Geochemistry, Geophysics, Geosystems*, *24*(5), e2022GC010844, doi:10.1029/2022GC010844.

Faccenna, C., Glišović, P., Forte, A., Becker, T. W., Garzanti, E., Sembroni, A. and Gvirtzman, Z. (2019). Role of dynamic topography in sustaining the Nile River over 30 million years. *Nature Geoscience*, *12*(12), 1012-1017, doi:10.1038/s41561-019-0472-x.

Fenneman, N. (1928). Physiographic Divisions of the United States. *Annals of the Association of American Geographers*, *18*(4), 261-353, doi:10.2307/2560726.

Fernandes, V.M., Roberts, G.G., White, N.J., and Whittaker, A.C. (2019). Continental-Scale Landscape Evolution: A History of North American Topography. *Journal of Geophysical Research: Earth Surface*, *124*, 2689-2722, doi:10.1029/2018JF004979.

Fernandes, V.M., and Roberts, G.G. (2021). Cretaceous to Recent Net Continental Uplift from Paleobiological Data: Insights into Sub-Plate Support. *Geological Society of America Bulletin*, *133*(5-6), 1217-1236,doi:10.1130/B35739.1.

Fitton, J.G., James, D., and Leeman, W.P. (1991). Basic magmatism associated with Late Cenozoic extension in the western United States: Compositional variations in space and time. *Journal of Geophysical Research*, *96*(B8), 13693, doi:10.1029/91JB00372.

Flament, N., Gurnis, M. and Müller, R.D. (2013). A review of observations and models of dynamic topography. *Lithosphere*, *5*2, 189-210, doi:10.1130/L245.1.

Flament, N., Williams, S., Müller, R., Gurnis, M. & Bower, D. (2017). Origin and evolution of the deep thermochemical structure beneath Eurasia. *Nature Communications*, *8*, 14164, doi:10.1038/ncomms14164.

Flowers, R.M., Wernicke, B.P., and Farley, K.A. (2008). Unroofing, incision, and uplift history of the southwestern Colorado Plateau from apatite (U-Th)/He thermochronometry. *GSA Bulletin*, *120*(5-6), 571-587, doi:10.1130/B26231.1.

Flowers, R.M., Ault, A.K., Kelley, S.A., Zhang, N., and Zhong, S. (2012). Epeirogeny or eustasy? Paleozoic-Mesozoic vertical motion of the North American continental interior from thermochronometry and implications for mantle dynamics. *Earth and Planetary Science Letters*, *317-318*, 436-445, doi:10.1016/j.epsl.2011.11.015.

Flowers, R.M., and Farley, K.A. (2012). Apatite ^{4}He/^{3}He and (U-Th)/He Evidence for an Ancient Grand Canyon. *Science*, *338*, 1616-1619, doi:10.1126/science.1229390.

Forte, A.M., Peltier, W.R., Dziewonski, A.M., and Woodward, R.L. (1993). Dynamic surface topography: A new interpretation based upon mantle flow models derived from seismic tomography. *Geophysical Research Letters*, *20*(3), 225-228, doi:10.1029/93GL00249.

Forte, A.M. (2000). Seismic-Geodynamic Constraints on Mantle Flow: Implications for Layered Convection, Mantle Viscosity, and Seismic Anisotropy in the Deep Mantle, *in* Karato, S.I., Forte, A., Liebermann, R., Masters, G., and Stixrude, L. (eds.) *Earth's Deep Interior: Mineral Physics and Tomography From the Atomic to the Global Scale*. American Geophysical Union–Geophysical Monograph Series, *117*, doi:10.1029/GM117p0003.

Forte, A.M., Mitrovica, J.X., Moucha, R., Simmons, N.A., and Grand, S.P. (2007). Descent of the ancient Farallon slab drives localized mantle flow below the New Madrid seismic zone. *Geophysical Research Letters*, *34*(4), doi:10.1029/2006GL027895.

Forte, A.M., Moucha, R., Simmons, N.A., Grand S.P., and Mitrovica, J.X. (2009). Deep-mantle contributions to the surface dynamics of the North American continent. *Tectonophysics*, *481*(1–4), 3-15, doi:10.1016/j.tecto.2009.06.010.

Forte, A.M., Quéré, S., Moucha, R., Simmons, N. A., Grand, S.P., Mitrovica, J.X., and Rowley, D.B. (2010). Joint seismic–geodynamic-mineral physical modelling of African geodynamics: A reconciliation of deep-mantle convection with surface geophysical constraints. *Earth and Planetary Science Letters*, *295*(3–4), 329-341, doi:10.1016/j.epsl.2010.03.017.

Galloway, W.E., Whiteaker, T.L., and Ganey-Curry, P. (2011). History of Cenozoic North American drainage basin evolution, sediment yield, and accumulation in the Gulf of Mexico basin. *Geosphere*, *7*(4), 938-973, doi:10.1130/GES00647.1.

Gani, R.M., Ranson, A., Cross, D.B., Hampson, G.J., Gani, N.D., and Sahoo, H. (2015). Along-strike sequence stratigraphy across the Cretaceous shallow marine to coastal-plain transition, Wasatch Plateau, Utah, U.S.A.. *Sedimentary Geology*, *325*, 59-70, doi:10.1016/j.sedgeo.2015.05.003.

Ghelichkhan, S., Bunge, H., and Oeser, J. (2021). Global mantle flow retrodictions for the early Cenozoic using an adjoint method: evolving dynamic topographies, deep mantle structures, flow trajectories and sublithospheric stresses. *Geophysical Journal International*, *226*, 1432–1460. doi:10.1093/gji/ggab108.

Gradstein, F.M., Ogg, J.G., Schmitz, M.B., and Ogg, G.M. (eds.) (2012). *The geologic time scale*, Elsevier, Oxford, UK.

Gurnis, M. (1988). Large-scale mantle convection and the aggregation and dispersal of supercontinents. *Nature*, *332*(6166), 695-699, doi:10.1038/332695a0.

Gurnis, M. (1990). Bounds on global dynamic topography from Phanerozoic flooding of continental platforms, *Nature*, *344*, 754-756, doi:10.1038/344754a0.

Gurnis, M. (1993). Phanerozoic marine inundation of continent driven by dynamic topography above subducting slabs, *Nature*, *364*, 590-593, doi:10.1038/364589a0.

978 Gurnis, M., Mitrovica, J.X., Ritsema, J., and van Heijst, H.J. (2000). Constraining mantle
979 density structure using geological evidence of surface uplift rates: The case of the African
980 Superplume. *Geochemistry, Geophysics Geosystems*, *1*(7), doi:10.1029/1999GC000035.
981 Gurnis, M., Turner, M., Zahirovic, S., DiCaprio, L., Spasojevic, S., Müller, R., Boyden, J., Se-
982 ton, M., Manea, V., and Bower, D. (2012). Plate tectonic reconstructions with continuously
983 closing plates, *Computers and Geosciences*, *38*, 35–42, doi:10.1016/j.cageo.2011.04.014.
984 Hager, B. H., Clayton, R. W., Richards, M. A., Comer, R. P., and Dziewonski, A. M. (1985).
985 Lower mantle heterogeneity, dynamic topography and the geoid. *Nature*, *313*(6003), 541-545,
986 doi:10.1038/313541a0.
987 Hager, B. H., and Richards, M. A. (1989). Long-wavelength variations in Earth's geoid:
988 physical models and dynamical implications. *Philosophical Transactions of the Royal*
989 *Society of London. Series A, Mathematical and Physical Sciences*, *328*(1599), 309-327,
990 doi:10.1098/rsta.1989.0038.
991 Hampson, G.J., (2010). Sediment dispersal and quantitative stratigraphic architecture across an
992 ancient shelf. *Sedimentology*, *57*, 96-141, doi:10.1111/j.1365-3091.2009.01093.x.
993 Hartley, R. A., Roberts, G. G., White, N., and Richardson, C. (2011). Transient convective up-
994 lift of an ancient buried landscape. *Nature Geoscience*, *4*(8), 562-565, doi:10.1038/ngeo1191.
995 Hassan, R., Flament, N., Gurnis, M., Bower, D.J., and Müller, D. (2015). Provenance of plumes
996 in global convection models, *Geochemistry, Geophysics, Geosystems*, *16*, 1465-1489.
997 Hazzard, J. A., Richards, F. D., Goes, S. D., and Roberts, G. G. (2023). Probabilistic assess-
998 ment of Antarctic thermomechanical structure: Impacts on ice sheet stability. *Journal of*
999 *Geophysical Research: Solid Earth*, *128*(5), e2023JB026653, doi:10.1029/2023JB026653.
1000 Heine, C., Yeo, L.G., and Müller, R.D. (2015). Evaluating global paleoshoreline models
1001 for the Cretaceous and Cenozoic. *Australian Journal of Earth Sciences*, *62*(3), 275-287,
1002 doi:10.1080/08120099.2015.1018321.
1003 Hernández-Uribe, D., and Palin, R. M. (2019). Catastrophic shear-removal of subcontinental
1004 lithospheric mantle beneath the Colorado Plateau by the subducted Farallon slab. *Scientific*
1005 *Reports*, *9*(1), 8153, doi:10.1038/s41598-019-44628-y.
1006 Hintze, L., and Kowallis, B. (2009). Geologic history of Utah, *Brigham Young University Geol-*
1007 *ogy Studies Special Publication 9*, Brigham Young University, Salt Lake City, UT.
1008 Hoggard, M. J., White, N. and Al-Attar, D. (2016). Global dynamic topography observa-
1009 tions reveal limited influence of large-scale mantle flow. *Nature Geoscience*, *9*, 456-463,
1010 doi:10.1038/10.1038/ngeo2709.
1011 Hoggard, M. J., Czarnota, K., Richards, F. D., Huston, D. L., Jaques, A. L., and Ghelichkhan,
1012 S. (2020). Global distribution of sediment-hosted metals controlled by craton edge stability.
1013 *Nature Geoscience*, *13*(7), 504-510, doi: 10.1038/s41561-020-0593-2.
1014 Hoggard, M., Austermann, J., Randel, C. and Stephenson, S. (2021). Observational Es-
1015 timates of Dynamic Topography Through Space and Time, in *Mantle Convection*
1016 *and Surface Expressions*, H. Marquardt, M. Ballmer, S. Cottaar and J. Konter (eds.),
1017 doi:10.1002/9781119528609.ch15.
1018 Holdt, M. C., White, N. J., Stephenson, S. N., and Conway-Jones, B. W. (2022). Densely sam-
1019 pled global dynamic topographic observations and their significance. *Journal of Geophysical*
1020 *Research: Solid Earth*, *127*(7), e2022JB024391, doi:10.1029/2022JB024391.
1021 Hunter, W. C., and Smith, D. (1981). Garnet peridotite from Colorado Plateau ultramafic dia-
1022 tremes: hydrates, carbonates, and comparative geothermometry. Contributions to Mineralogy
1023 and Petrology, 76, 312-320.
1024 Huntington, K.W., Wernicke, B.P., and Eiler, J.M. (2010). Influence of climate change and up-
1025 lift on Colorado Plateau paleotemperatures from carbonate clumped isotope thermometry,
1026 *Tectonics*, *29*(3), 1-19, doi:10.1029/2009TC002449.
1027 Jarvis, A., H.I. Reuter, A. Nelson, and E. Guevara (2008). Hole-filled SRTM for the globe Ver-
1028 sion 4, *CGIAR-CSI SRTM 90m Database*, http://srtm.csi.cgiar.org.
1029 Johnson, K.R., Nichols, D.J., and Hartman, J.H. (2002). Hell Creek Formation: a 2001 synthe-
1030 sis, *in*, Hartman, J.H., Johnson, K.R., and Nichols, D.J. (eds.), The Hell Creek Formation
1031 and the Cretaceous-Tertiary boundary in the northern Great Plains: An integrated conti-
1032 nental record of the end of the Cretaceous, *Geological Society of America Special Paper 361*,

Boulder, CO., 503-510.

Katsura, T., Shatskiy, A., Manthilake, M.G.M., Zhai, S., Fukui, H., Yamazaki, D., Matsuzaki, T., Yoneda, A., Ito, E., Kuwata, A., Ueda, A., Nozawa, A., and Funakoshi, K. (2009). Thermal expansion of forsterite at high pressures determined by in situ X-ray diffraction: The adiabatic geotherm in the upper mantle. *Physics of the Earth and Planetary Interiors*, *174*(1-4), 86-92, doi:10.1016/j.pepi.2008.08.002.

Klöcking, M., White, N.J., Maclennan, J., McKenzie, D., and Fitton, J.G. (2018). Quantitative Relationships Between Basalt Geochemistry, Shear Wave Velocity, and Asthenospheric Temperature Beneath Western North America. Geochemistry, Geophysics, Geosystems, *19*(9), 3376-3404, doi:10.1029/2018GC007559.

Lamb, S., Moore, J. D., Perez-Gussinye, M., and Stern, T. (2020). Global whole lithosphere isostasy: implications for surface elevations, structure, strength, and densities of the continental lithosphere. *Geochemistry, Geophysics, Geosystems*, *21*(10), e2020GC009150, doi:10.1029/2020GC009150.

Laske, G., Masters, G., Ma, Z., and Pasyanos, M. (2013). Update on CRUST1.0–A 1-degree global model of Earth's crust, *Geophysical Research Abstracts*, *15*, 2658, Vienna, Austria: EGU General Assembly.

Levandowski, W., Jones, C.H., Butcher, L.A., and Mahan, K.H. (2018). Lithospheric density models reveal evidence for Cenozoic uplift of the Colorado Plateau and Great Plains by lower-crustal hydration, *Geosphere*, *14*(3), 1-15, doi:10.1130/GES01619.1.

Li, Z., and Aschoff, J. (2022). Constraining the effects of dynamic topography on the development of Late Cretaceous Cordilleran foreland basin, western United States. *GSA Bulletin*, *134*(1-2), 446-462, doi:10.1130/B35838.1.

Lipp, A. G., and Roberts, G. G. (2021). Scale-dependent flow directions of rivers and the importance of subplate support. *Geophysical Research Letters*, *48*(1), e2020GL091107, doi:10.1029/2020GL091107.

Liu, L., Spasojević, S., and Gurnis, M. (2008). Reconstructing Farallon plate subduction beneath North America back to the Late Cretaceous. *Science*, *322*(January), 934-938, doi:10.5061/dryad.5t110.

Liu, S., Nummedal, D., and Gurnis, M. (2014). Dynamic versus flexural controls of Late Cretaceous Western Interior Basin, USA. *Earth and Planetary Science Letters*, *389*, 221-229, doi:10.1016/j.epsl.2014.01.006.

Liu, L., and Gurnis, M. (2008). Simultaneous inversion of mantle properties and initial conditions using an adjoint of mantle convection. *Journal of Geophysical Research: Solid Earth*, *113*, doi:10.1029/2008JB005594.

Lodhia, B. H., Roberts, G. G., Fraser, A. J., Fishwick, S., Goes, S., and Jarvis, J. (2018). Continental margin subsidence from shallow mantle convection: Example from West Africa. *Earth and Planetary Science Letters*, *481*, 350-361, doi:10.1016/j.epsl.2017.10.024.

Lynds, R.M., and Slattery, J.S. (2017). Correlation of the Upper Cretaceous strata of Wyoming, *Wyoming State Geological Survey.*

McKenzie, D. P., Roberts, J. M., and Weiss, N. O. (1974). Convection in the Earth's mantle: towards a numerical simulation. *Journal of Fluid Mechanics*, *62*(3), 465-538, doi:10.1017/S0022112074000784.

McKenzie, D., and Jarvis, G. (1980). The conversion of heat into mechanical work by mantle convection. *Journal of Geophysical Research: Solid Earth*, *85*(B11), 6093-6096, doi:10.1029/JB085iB11p06093.

McKenzie, D. (1978). Some remarks on the development of sedimentary basins. *Earth and Planetary Science Letters*, *40*(1), 25-32, doi:10.1016/0012-821X(80)90168-5.

McKenzie, D., Jackson, J., and Priestley, K. (2005). Thermal structure of oceanic and continental lithosphere. *Earth and Planetary Science Letters*, *233*(3-4), 337-349, doi:10.1016/j.epsl.2005.02.005.

Menard, H. W. (1969). Elevation and subsidence of oceanic crust. *Earth and Planetary Science Letters*, *6*, 4, 275-284, doi:10.1016/0012-821X(69)90168-X.

Merewether, E.A., Cobban, W.A., and Obradovich, J.D. (2011). Biostratigraphic Data from Upper Cretaceous Formations–eastern Wyoming, Central Colorado, and Northeastern New

Mexico, *U.S. Geological Survey Scientific Investigations Map 3175*, 2 sheets, pamphlet, 10 p.

Merewether, E.A., and McKinney, K.C. (2015). Composite biostratigraphic outcrop sections for Cretaceous Formations along a south-trending transect from northwestern Montana to northwestern New Mexico, *USGS*, *1258*, 20151, 087.

Mitrovica, J.X., Beaumont, C., and Jarvis, G.T. (1989). Tilting of continental interiors by the dynamical effects of subduction, *Tectonics*, *8*(5), 1079-1094, doi:10.1029/TC008i005p01079.

Mooney, W. D., and Kaban, M. K. (2010). The North American upper mantle: Density, composition, and evolution. *Journal of Geophysical Research: Solid Earth*, *115*(B12), doi:10.1029/2010JB000866.

Morris, M., Fernandes, V. M., and Roberts, G. G. (2020). Extricating dynamic topography from subsidence patterns: Examples from Eastern North America's passive margin. *Earth and Planetary Science Letters*, *530*, 115840, doi:10.1016/j.epsl.2019.115840.

Moucha, R., Forte, A. M., Rowley, D. B., Mitrovica, J. X., Simmons, N. A., and Grand, S. P. (2008). Mantle convection and the recent evolution of the Colorado Plateau and the Rio Grande Rift valley. *Geology*, *36*(6), 439-442. doi:10.1130/G24577A.1.

Moucha, R., Forte, A. M., Mitrovica, J. X., Rowley, D. B., Quéré, S., Simmons, N. A., and Grand, S. P. (2008). Dynamic topography and long-term sea-level variations: There is no such thing as a stable continental platform. *Earth and Planetary Science Letters*, *271*(1), 101-108. doi:10.1016/j.epsl.2008.03.056.

Müller, R.D., Flament, N., Matthews, K.J., Williams, S.E., and Gurnis, M. (2016a). Formation of Australian continental margin highlands driven by plate–mantle interaction, *Earth and Planetary Science Letters*, *441*, 60–70, doi:10.1016/j.epsl.2016.02.025.

Müller, R.D., Seton, M., Zahirovic, S., Williams, S.E., Matthews, K.J., Wright, N.M., Shephard, G., Maloney, K.T., Barnett-Moore, N., Hosseinpour, M., Bower, D.J., and Cannon, J. (2016b). Ocean basin evolution and global-scale plate reorganization events since Pangea breakup, *Annual Review of Earth and Planetary Science*s, 44, 107–138, doi:10.1146/annurev-earth-060115-012211.

Müller, R.D., Hassan, R., Gurnis, M., Flament, N., and Williams, S.E. (2018). Dynamic topography of passive continental margins and their hinterlands since the Cretaceous, *Gondwana Research*, *53*, 225-251, doi:10.1016/j.gr.2017.04.028.

Obradovich, J.D., and Cobban, W.A. (1975). A time-scale for the Late Cretaceous of the Western Interior of North America, *Geological Association of Canada Special Paper 13*, 31-54.

Parsons, B. and Daly, S. (1983). The relationship between surface topography, gravity anomalies, and temperature structure of convection. *Journal of Geophysical Research*, *88*(B2), 1129-1144, doi:10.1029/JB088iB02p01129.

Parsons, B., and Sclater, J. G. (1977). An analysis of the variation of ocean floor bathymetry and heat flow with age. *Journal of Geophysical Research*, *82*(5), 803-827, doi:10.1093/petrology/29.3.625.

Panasyuk, S. V. and Hager, B. H. (2000). Inversion for mantle viscosity profiles constrained by dynamic topography and the geoid, and their estimated errors. *Geophysical Journal International*, *143*(3), 821-836, doi:10.1046/j.0956-540X.2000.01286.x.

Pang, M., and Nummedal, D. (1995). Flexural subsidence and basement tectonics of the Cretaceous Western Interior basin, United States. *Geology*, *23*(2), 173-176, doi:10.1130/0091-7613(1995)023<0173:FSABTO>2.3.CO;2.

Pekeris, C. L. (1935). Thermal convection in the interior of the Earth. *Geophysical Journal International*, *3*, 343-367, doi:10.1111/j.1365-246X.1935.tb01742.x.

Richards, M. A., and Hager, B. H. (1984). Geoid anomalies in a dynamic Earth. *Journal of Geophysical Research: Solid Earth*, *89*(B7), 5987-6002, doi:10.1029/JB089iB07p05987.

Richards, F. D., Coulson, S. L., Hoggard, M. J., Austermann, J. A., Dyer, B., and Mitrovica, J. X. (2023). Geodynamically corrected Pliocene shoreline elevations in Australia consistent with midrange projections of Antarctic ice loss. *Science Advances*, *9*(46), eadg3035, doi:10.1126/sciadv.adg3035.

Richards, F.D., Hoggard, M.J., White, N., and Ghelichkhan, S. (2020). Quantifying the relationship between short-wavelength dynamic topography and thermomechanical structure of the upper mantle using calibrated parameterization of anelasticity. *Journal of Geophysical*

Research: Solid Earth, *125*(9), e2019JB019062, doi:10.1029/2019JB019062.

Richards, F., Hoggard, M., Crosby, A., Ghelichkhan, S., and White, N. (2020). Structure and dynamics of the oceanic lithosphere-asthenosphere system. *Physics of the Earth and Planetary Interiors*, *309*, 106559, doi:10.1016/j.pepi.2020.106559.

Riter, J. C. A., & Smith, D. (1996). Xenolith constraints on the thermal history of the mantle below the Colorado Plateau. *Geology*, *24*(3), 267-270, doi:10.1130/0091-7613(1996)024<0267:XCOTTH>2.3.CO;2.

Richards, F. D., Hoggard, M. J., Cowton, L. R., and White, N. J. (2018). Reassessing the thermal structure of oceanic lithosphere with revised global inventories of basement depths and heat flow measurements. *Journal of Geophysical Research: Solid Earth*, *123*(10), 9136-9161, doi:10.1029/2018JB015998.

Roberts, L.N.R., and Kirschbaum, M.A. (1995). Paleogeography and the Late Cretaceous of the Western Interior of middle North America; coal distribution and sediment accumulation. *USGS Professional Paper 1561*, doi:10.3133/pp1561.

Roberts, G. G., Paul, J. D., White, N., and Winterbourne, J. (2012). Temporal and spatial evolution of dynamic support from river profiles: A framework for Madagascar. *Geochemistry, Geophysics, Geosystems*, *13*(4), doi:10.1029/2012GC004040.

Roberts, G.G., White, N.J., Martin-Brandis, G.L., and Crosby, A.G. (2012a), An uplift history of the Colorado Plateau and its surroundings from inverse modeling of longitudinal river profiles, *Tectonics*, *31*(4), 1-25, doi:10.1029/2012TC003107.a.

Roy, M., Jordan, T.H., and Pederson, J.L. (2009). Colorado Plateau magmatism and uplift by warming of heterogeneous lithosphere. *Nature*, *459*(7249), 978-82, doi:10.1038/nature08052.

Rovere, A., Hearty, P. J., Austermann, J., Mitrovica, J. X., Gale, J., Moucha, R., Forte, A.M. and Raymo, M.E. (2015). Mid-Pliocene shorelines of the US Atlantic Coastal Plain—An improved elevation database with comparison to Earth model predictions. *Earth-Science Reviews*, *145*, 117-131, doi:10.1016/j.earscirev.2015.02.007.

Rowley, D. B., Forte, A. M., Moucha, R., Mitrovica, J. X., Simmons, N. A., and Grand, S. P. (2013). Dynamic topography change of the eastern United States since 3 million years ago. *Science*, *340*(6140), 1560-1563, doi:10.1126/science.1229180.

Rudge, J.F., Champion, M.E.S., White, N., McKenzie, D., and Lovell, B. (2008). A plume model of transient diachronous uplift at the Earth's surface. *Earth and Planetary Science Letters*, *267*(1–2), 146-160, doi:10.1016/j.epsl.2007.11.040.

Sahagian, D. (1988). Epeirogenic motions of Africa as inferred from Cretaceous shoreline deposits. *Tectonics*, *7*(1), 125-138, doi:10.1029/TC007i001p00125.

Salles, T., Flament, N., and Müller, D. (2017). Influence of mantle flow on the drainage of eastern A ustralia since the Jurassic Period. *Geochemistry, Geophysics, Geosystems*, *18*(1), 280-305, doi:10.1002/2016GC006617.

Sclater, J.G., and Christie, P.A.F. (1980). Continental stretching: An explanation for the post-Mid-Cretaceous subsidence of the Central North Sea Basin, *Journal of Geophysical Research: Solid Earth*, *85*(B7), 3711-3739, doi:10.1029/JB085iB07p03711.

Schaeffer, A.J., and Lebedev, S. (2013). Global shear speed structure of the upper mantle and transition zone. *Geophysical Journal International*, *194*(1), 417-449, doi:10.1093/gji/ggt095.

Schaeffer, A.J. and Lebedev, S. (2014). Imaging the North American continent using waveform inversion of global and USArray data, *Earth and Planetary Science Letters*, *402*, 26-41, doi:10.1016/j.epsl.2014.05.014.

Schutt, D. L., and Lesher, C. E. (2006). Effects of melt depletion on the density and seismic velocity of garnet and spinel lherzolite. *Journal of Geophysical Research: Solid Earth*, *111*(B5), doi:10.1029/2003JB002950.

Seton, M., Müller, R.D., Zahirovic, S., Gaina, C., Torsvik, T.H., Shephard, G., Talsma, A., Gurnis, M., Turner, M., Maus, S., and Chandler, M.T. (2012). Global continental and ocean basin reconstructions since 200 Ma. *Earth Science Reviews*, *113*, 212–270, doi:10.1016/j.earscirev.2012.03.002.

Shephard, G., Müller, R.D. and Seton, M. (2013). The tectonic evolution of the Arctic since Pangea breakup: Integrating constraints from surface geology and geophysics with mantle structure. *Earth Science Reviews*, *124*, 148-183, doi:10.1016/j.earscirev.2013.05.012.

Shephard, G., Flament, N., Williams, S., Seton, M., Gurnis, M. and Müller, R.D. (2014). Circum-Arctic mantle structure and long-wavelength topography since the Jurassic. *Journal of Geophysical Research: Solid Earth*, *119*(10), 7889-7908, doi:10.1002/2014JB011078.

Smith, A.G., Smith, D.G., and Funnell, B.M. (1994). *Atlas of Mesozic and Cenozoic Coastlines*, 99 pp., Cambridge University Press.

Spasojević, S., and Gurnis, M. (2012). Sea level and vertical motion of continents from dynamic earth models since the Late Cretaceous. *AAPG Bulletin*, *96*(11), 2037-2064, doi:10.1306/03261211121.

Stephenson, S.N., Roberts, G.G., Hoggard, M.J., and Whittaker, A.C. (2014), A Cenozoic uplift history of Mexico and its surroundings from longitudinal river profiles. *Geochemistry, Geophysics, Geosystems*, *15*(12), 4734-4758, doi:10.1002/2014GC005425.

Stephenson, S. N., White, N. J., Li, T., and Robinson, L. F. (2019). Disentangling interglacial sea level and global dynamic topography: Analysis of Madagascar. *Earth and Planetary Science Letters*, *519*, 61-69, doi:10.1016/j.epsl.2019.04.029.

Stephenson, S., Hoggard, M., and White, N. (2021, April). Global continental residual topography. In EGU general assembly conference abstracts (pp. EGU21-15505).

Valentine, A. P., and D. R. Davies (2020). Global Models From Sparse Data: A Robust Estimate of Earth's Residual Topography Spectrum. *Geochemistry, Geophysics, Geosystems*, *21*(8), e2020GC009.240, doi:10.1029/2020GC009240.

Van Der Meer, D.G., Spakman, W., Van Hinsbergen, D.J., Amaru, M.L., and Torsvik, T.H. (2010). Towards absolute plate motions constrained by lower-mantle slab remnants, *Nature Geoscience*, *3*, 36-40, doi:10.1038/ngeo708.

Walker, J.D., Todd, D.B., Ross, A.B., Glazner, A., Farmer, L., and Richard, W. (2006). NAVDAT: A western North American volcanic and intrusive rock geochemical database, *Special Paper of the Geological Society of America*, *397*, doi:10.1130/2006.2397(05).

Wang, H., Gurnis, M., & Skogseid, J. (2020). Continent-wide drainage reorganization in North America driven by mantle flow. *Earth and Planetary Science Letters*, *530*, 115910. doi: 10.1016/j.epsl.2019.115910.

Watts, A. B. (2001). Isostasy and Flexure of the Lithosphere. *Cambridge University Press.*

Yamauchi, H., and Takei, Y. (2016). Polycrystal anelasticity at near-solidus temperatures. *Journal of Geophysical Research: Solid Earth*, *121*(11), 7790-7820, doi:10.1002/2016JB013316.

Ziegler, A., Rowley, D., Lottes, A., Sahagian, D., Hulver, M., and Gierlowski, T. (1985). Paleogeographic interpretation: with an example from the mid-Cretaceous, *Annual Review of Earth and Planetary Science*, *13*, 385-425, doi:10.1146/annurev.earth.13.1.385.